The Materials Science of Thin Films



Milton Ohring

Infineon Exhibit 2031
Innoscience v. Infineon
IPR2025-00175

The Materials Science *of* Thin Films

Milton Ohring

Stevens Institute of Technology
Department of Materials Science and Engineering
Hoboken, New Jersey



Academic Press
San Diego New York Boston
London Sydney Tokyo Toronto

This book is printed on acid-free paper. ♾

Copyright © 1992 by Academic Press
All rights reserved.
No part of this publication may be reproduced or transmitted in any form or by any means, electronic or mechanical, including photocopy, recording, or any information storage and retrieval system, without permission in writing from the publisher.

Designed by Elizabeth E. Tustian

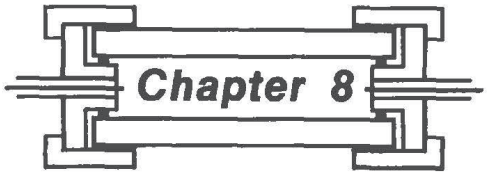
ACADEMIC PRESS
A Division of Harcourt Brace & Company
525 B Street, Suite 1900, San Diego, California 92101-4495

United Kingdom Edition published by
ACADEMIC PRESS LIMITED
24-28 Oval Road, London NW1 7DX

Library of Congress Cataloging-in-Publication Data

Ohring, Milton, date.
The materials science of thin films / Milton Ohring.
p. cm.
Includes bibliographical references and index.
ISBN 0-12-524990-X (Alk. paper)
1. Thin films. I. Title.
TA418.9.T45047 1991
620'.44—dc20 91-9664
CIP

Printed in the United States of America
99 00 01 02 03 MV 11 10 9 8 7



Interdiffusion and Reactions in Thin Films

8.1. Introduction

There is hardly an area related to thin-film formation, properties, and performance that is uninfluenced by mass-transport phenomena. This is especially true of microelectronic applications, where very small lateral as well as depth dimensions of device features and film structures are involved. When these characteristic dimensions (d) become comparable in magnitude to atomic diffusion lengths, then compositional changes can be expected. New phases such as precipitates or layered compounds may form from ensuing reactions, altering the initial film integrity. This, in turn, frequently leads to instabilities in the functioning of components and devices that are manifested by such effects as decrease in conductivity as well as short- or even open-circuiting of conductors, lack of adhesion, and generation of stress. The time it takes for such effects to evolve can be roughly gauged by noting that the diffusion length is given by $\sim 2\sqrt{Dt}$, where D and t are the appropriate diffusivity and time, respectively. Therefore $t \approx d^2/4D$. As we shall see, D values in films are relatively high even at low temperatures, so small film dimensions serve to make these characteristic times uncomfortably short. Such problems frequently surface when neighboring combinations of materials are chemically reactive.

For example, consider the the pitfalls involved in designing a Cu–Ni film couple as part of the contact structure for solar cells (Ref. 1). Readily available high-temperature data in *bulk* metals extrapolated to 300 °C yield a value of 3.8×10^{-24} cm^2/sec for the diffusion coefficient of Cu in Ni. For a 1000Å thick Ni film, the interdiffusion time is thus predicted to be $(10^{-5})^2/4(3.8 \times 10^{-24})$ sec, or over 200,000 years! Experiment, however, revealed that these metals intermixed in less than an hour. When colored metal films are involved, as they are here, the eye can frequently detect the evidence of interdiffusion through color or reflectivity changes. The high density of defects, e.g., grain boundaries and vacancies, causes deposited films to behave differently from bulk metals, and it is a purpose of this chapter to quantitatively define the distinctions. Indeed, a far more realistic estimate of the Cu–Ni reaction time can be made by utilizing the simple concepts developed in Section 8.2. Other examples will be cited involving interdiffusion effects between and among various metal film layer combinations employed in Si chip packaging applications. Practical problems associated with making both stable contacts to semiconductor surfaces and reliable interconnections between devices have been responsible for generating the bulk of the mass-transport-related concerns and studies in thin films. For this reason, issues related to these extremely important subjects will be discussed at length.

While interdiffusion phenomena are driven by chemical concentration gradients, other mass-transport effects take place even in homogeneous films. These rely on other driving forces such as electric fields, thermal gradients, and stress fields, which give rise to respective electromigration, thermomigration, and creep effects that can similarly threaten film integrity. The Nernst–Einstein equation provides an estimate of the characteristic times required for such transport effects to occur. Consider a narrow film stripe that is as wide as it is thick. If it can be assumed that the volume of film affected is $\sim d^3$ and the mass flows through a cross-sectional area d^2, then the appropriate velocity is d/t. By utilizing Eq. 1-35, we conclude that $t \approx RTd/DF$. Large driving forces (F), which sometimes exist in films, can conspire with both small d and high D values to reduce the time to an undesirably short period. As circuit dimensions continue to shrink in the drive toward higher packing densities and faster operating speeds, diffusion lengths will decrease and the surface-area-to-volume ratio will increase. Despite these tendencies, processing temperatures and heat generated during operation are not being proportionately reduced. Therefore, interdiffusion problems are projected to persist and even worsen in the future.

In addition to what may be termed reliability concerns, there are beneficial mass-transport effects that are relied on during processing heat treatments in

films. Aspects of both of these broad applications will be discussed in this chapter in a fundamental way within the context of the following subjects:

8.2. Fundamentals of Diffusion
8.3. Interdiffusion in Metal Alloy Films
8.4. Electromigration in Thin Films
8.5. Metal–Semiconductor Reactions
8.6. Silicides and Diffusion Barriers
8.7. Diffusion During Film Growth

Before proceeding, the reader may find the survey of diffusion phenomena given in Chapter 1 useful and wish to review it.

8.2. Fundamentals of Diffusion

8.2.1. Comparative Diffusion Mechanisms

Diffusion mechanisms attempt to describe the details of atomic migration associated with mass transport through materials. The resulting atom movements reflect the marginal properties of materials in that only a very small fraction of the total number of lattice sites, namely, those that are unoccupied, interstitial, or on surfaces, is involved. An illustration of the vacancy mechanism for diffusion was given on p. 36. Similarly, the lattice diffusivity D_L, in terms of previously defined quantities, can be written as

$$D_L = D_0 \exp - E_L/RT, \tag{8-1}$$

where E_L is the energy for atomic diffusion through the lattice on a per-mole basis. In polycrystalline thin films the very fine grain size means that a larger proportion of atom-defect combinations is associated with grain boundaries, dislocations, surfaces, and interfaces, relative to lattice sites, than is the case in bulk solids. Less tightly bound atoms at these nonlattice sites are expected to attract different point-defect populations and be more mobile than lattice atoms. Although the detailed environment may be complex and even varied, the time-averaged atomic transport is characterized by the same type of Boltzmann behavior expressed by Eq. 8-1. Most importantly, the activation energies for grain-boundary, dislocation, and surface diffusion are expected to be smaller than E_L, leading to higher diffusivities. Therefore, such heterogeneities and defects serve as diffusion paths that short-circuit the lattice.

In order to appreciate the consequences of allowing a number of uncoupled transport mechanisms to freely compete, we consider the highly idealized

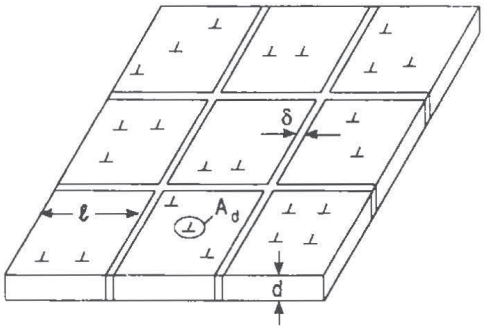


Figure 8-1. Highly idealized polycrystalline film containing square grains, grain boundaries, and dislocations.

polycrystalline film matrix in Fig. 8-1. Grain-boundary slabs of width δ serve as short-circuit diffusion paths even though they may only be 5–10 Å wide. They separate square-shaped grains of side l. Within the grains are dissociated dislocations oriented normal to the film surface. They thread the latter with a density ρ_d per cm^2, and diffusion is assumed to occur through the dislocation core whose cross-sectional area is A_d. Parallel transport processes normal to the film plane are assumed to occur for each mechanism. Under these conditions, the number of atoms ($\dot{n}_i$) that flow per unit time is essentially equal to the product of the appropriate diffusivity (D_i), concentration gradient $(dc/dx)_i$, and transport area involved. Therefore,

Lattice: $$\dot{n}_L = D_L l^2 \left(\frac{dc}{dx}\right)_L, \tag{8-2a}$$

Grain Boundary: $$\dot{n}_b = \delta D_b l \left(\frac{dc}{dx}\right)_b, \tag{8-2b}$$

Dislocation: $$\dot{n}_d = A_d D_d l^2 \rho_d \left(\frac{dc}{dx}\right)_d, \tag{8-2c}$$

where L, b and d refer to lattice, grain-boundary, and dislocation quantities.

The importance of short-circuit mass flow relative to lattice diffusion can be quantitatively understood in the case of face-centered cubic metals where data for the individual mechanisms are available. A convenient summary of resulting diffusion parameters is given by (Ref. 2)

Lattice: $$D_L \approx 0.5 \exp - 17.0 T_M / T \text{ cm}^2/\text{sec}, \tag{8-3a}$$

Grain Boundary: $$\delta D_b \approx 1.5 \times 10^{-8} \exp - 8.9 T_M / T \text{ cm}^3/\text{sec}, \tag{8-3b}$$

Dislocation: $$A_d D_d \approx 5.3 \times 10^{-15} \exp - 12.5 T_M / T \text{ cm}^4/\text{sec}. \tag{8-3c}$$

These approximate expressions represent average data for a variety of FCC metals normalized to the reduced temperature T/T_M, where T_M is the melting point. As an example, the activation energy for lattice self-diffusion in Au is easily estimated through comparison of Eqs. 8-1 and 8-3a, which gives $E_L/RT = 17.0T_M/T$. Therefore, $E_L = 17.0RT_M$ or (17.0)(1.99 cal/mole-K)(1336 K) = 45,200 cal/mole. As a first approximation, the preceding equations can be assumed to be valid for both self- and dilute impurity diffusion. Generalized Arrhenius plots for D_L as a function of T_M/T have already been introduced in Fig. 5-6 for metal, semiconductor, and alkali halide matrices.

Regimes of dominant diffusion behavior, normalized to the same concentration gradient, can be mapped as a function of l and ρ_d by equating the various $\dot{n}_i$ in Eq. 8-2. The equations of the boundary lines separating the operative transport mechanisms are thus

$$\frac{1}{l} = \frac{D_L}{\delta D_b}, \quad \rho_d = \frac{D_L}{A_d D_d}, \quad \text{and} \quad \frac{1}{l} = \frac{A_d D_d \rho_d}{\delta D_b}.$$

These are plotted as $\ln 1/l$ versus ρ_d in Fig. 8-2 at four levels of T/T_M,

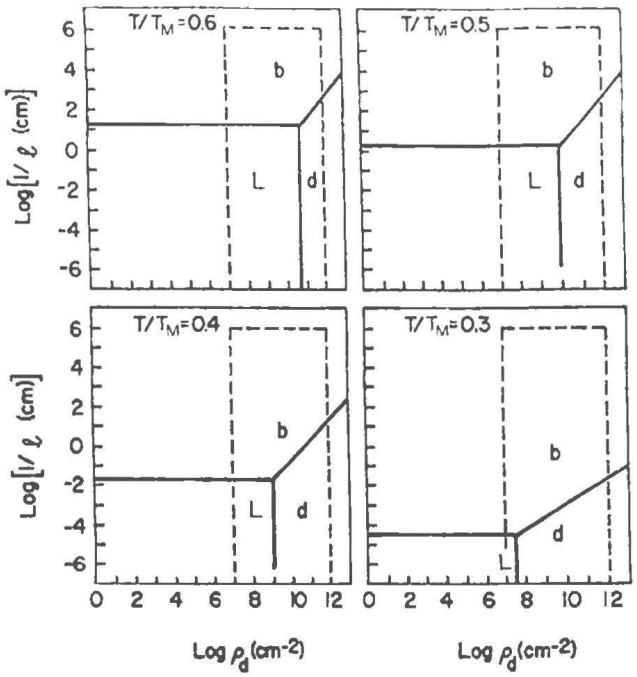


Figure 8-2. Regimes of dominant diffusion mechanisms in FCC metal films as a function of temperature. (Reprinted with permission from Elsevier Sequoia, S.A. from R. W. Balluffi and J. M. Blakely, *Thin Solid Films* **25**, 363, 1975).

employing Eqs. 8-3a, b, c. The broken rectangles represent the range of thin film values for l and ρ_d that occur in practice. For typical metal films with a grain size of 1 μm or less, grain-boundary diffusion dominates at all practical temperatures. Similarly, for dislocation-free epitaxial films where $1/l = 0$, lattice diffusion dominates. Transport at these extremes is intuitively obvious. Where the film structure is such that combinations of mechanisms are operative, different admixtures will occur as a function of temperature. Generally, lower temperatures will favor grain boundary and dislocation short-circuiting relative to lattice diffusion.

Surface diffusion is another transport mechanism of relevance to thin films because of the large ratio of the number of surface-to-bulk atoms. As noted in Chapter 5, this mechanism plays an important role in film nucleation and

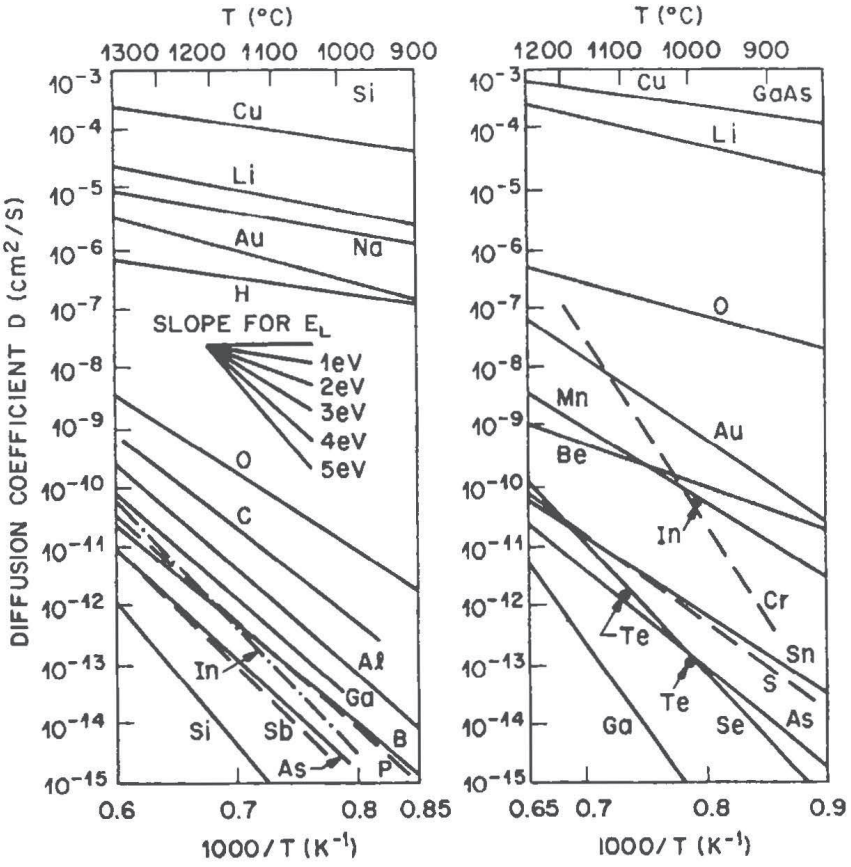


Figure 8-3. Diffusion coefficients of various elements in Si and GaAs as a function of temperature. (Reprinted with permission from John Wiley and Sons, from S. M. Sze, *Semiconductor Devices: Physics and Technology*, Copyright © 1985, John Wiley and Sons).

growth processes. Reduced parameters describing measured surface transport in FCC metals have been suggested (Ref. 3); e.g.,

$$D_s \approx 0.014 \exp - \frac{6.54 T_M}{T} \text{ cm}^2/\text{sec} \qquad \text{for } \frac{T_M}{T} > 1.3.$$

It is well known, however, that surface diffusion varies strongly with ambient conditions, surface crystallography, and the nature and composition of surface and substrate atoms.

Systematics similar to those depicted in Fig. 8-2 also govern diffusion behavior in ionic solids and semiconductors where grain boundaries and dislocations are known to act as short-circuit paths. However, complex space-charge effects in ionic solids make a clear separation of lattice and grain-boundary diffusion difficult in these materials. In semiconductors a great deal of impurity diffusion data exists, and these are used in designing and analyzing doping treatments for devices. This is a specialized field, and complex modeling (Ref. 4) is required to accurately describe diffusion profiles. Due to the importance of Si and GaAs films, preferred lattice dopant diffusion data are presented in Fig. 8-3 (Ref. 5). Some very recent data on diffusion of noble metals Au, Ag, and Cu in amorphous Si films interestingly reveals that the activation energy for diffusion in the disordered matrix is very similar to values obtained for lattice diffusion in crystalline Si. (Ref. 6).

8.2.2. Grain-Boundary Diffusion

Of all the mass-transport mechanisms in films, grain-boundary (GB) diffusion has probably received the greatest attention. This is a consequence of the rather small grain size and high density of boundaries in deposited films. Rapid diffusion within individual GBs coupled with their great profusion make them the pathways through which the major amount of mass is transported. Low diffusional activation energies foster low-temperature transport, creating serious reliability problems whose origins can frequently be traced to GB involvement. This has motivated the modeling of both GB diffusion and phenomena related to film degradation processes.

The first treatment of GB diffusion appeared nearly 40 years ago. The Fisher model (Ref. 7) of GB diffusion considers transport within a semi-infinite bicrystal film initially free of diffusant, as shown in Fig. 8-4. A diffusant whose concentration C_0 is permanently maintained at plane $y = 0$ diffuses into the GB and the two adjoining grains. At low temperatures in typical polycrystalline films, it is easily shown that there is far more transport down

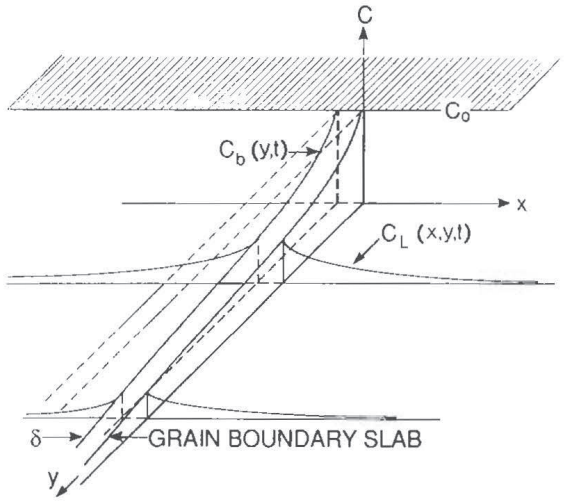


Figure 8-4. Representation of diffusional penetration down a grain boundary (y direction) with simultaneous lateral diffusion into adjoining grains (x direction).

the GB than there is into the matrix of the grains. The ratio of these two fluxes can be estimated through the use of Eqs. 8-2 and 8-3 for FCC metals; i.e.,

$$\frac{\dot{n}_b}{\dot{n}_L} = \frac{\delta D_b}{lD_L} = \frac{3 \times 10^{-8}}{l} \exp \frac{8.1\, T_M}{T}.$$

Assuming $l = 10^{-4}$ cm and $T/T_M = 1/3$, we have $\dot{n}_b/\dot{n}_l = 1.1 \times 10^7$. For this reason, we may envision transport to consist primarily of a deep rapid penetration down the GB from which diffusant subsequently diffuses laterally into the adjoining grains, building up the concentration level there. This is shown schematically in Fig. 8-4 and described mathematically by

$$C_L(x, y, t) = C_0 \exp - \left(\frac{2\sqrt{D_L}}{\delta D_b \sqrt{\pi t}} \right)^{1/2} y \cdot \operatorname{erfc} \frac{x}{2\sqrt{D_L t}}, \qquad (8\text{-}4)$$

where $C_L(x, y, t)$ is the diffusant concentration at any position and time.

The Fisher analysis of the complex, coupled GB–lattice diffusion process yields simplified decoupled solutions—an exponential diffusant profile in the GB and an error function profile within adjoining grains. Experimental verification of Eq. 8-4 is accomplished by measurement of the integrated concentration $\bar{C}$ within incremental slices Δy thick (e.g., by sputtering) normal to the $y = 0$ surface; i.e.,

$$\bar{C} = \int_{-\infty}^{\infty} C_L(x, y, t)\, dx\, \Delta y = \text{const}\; e^{-(2\sqrt{D_L}/\delta D_b \sqrt{\pi t})^{1/2} y}. \qquad (8\text{-}5)$$

The last equation suggests that a plot of $\ln \bar{C}$ versus y is linear. Therefore, the useful result

$$\delta D_b = \frac{1.0}{\sqrt{\pi}} \left(\frac{d \ln \bar{C}}{dy} \right)^{-2} \left(\frac{4 D_L}{t} \right)^{1/2} \tag{8-6}$$

emerges. However, in order to obtain δD_b, the value of D_L in the same system must be independently known. This poses no problem usually, since lattice diffusivity data are relatively plentiful. Exact, but far more complicated, integral solutions, that are free of the simplifications of the Fisher analysis, have been obtained by Whipple (Ref. 8) and Suzuoka (Ref. 9). A conclusion, based on these analyses, that has been extensively used is

$$\delta D_b = -0.66 \left(\frac{d \ln \bar{C}}{dy^{6/5}} \right)^{-5/3} \left(\frac{4 D_L}{t} \right)^{1/2}. \tag{8-7}$$

Apart from overriding questions of correctness, the difference between Eqs. 8-6 and 8-7 is that $\ln \bar{C}$ is plotted versus y in the former and versus $y^{6/5}$ in the latter. Frequently, however, the experimental concentration profiles are not sufficiently precise to distinguish between these two spatial dependencies. It does not matter that actual films are not composed of bicrystals, but rather polycrystals with GBs of varying type and orientation; the general character of the solutions is preserved despite the geometric complexity. A schematic representation of equiconcentration profiles in a polycrystalline film containing an array of parallel GBs is shown in Fig. 8-5. At elevated temperatures the extensive amount of lattice diffusion masks the penetration through GBs. At the lowest temperatures, virtually all of the diffusant is partitioned to GBs. In between, the admixture of diffusion mechanisms results in an initial rapid penetration down the short-circuit network, which slows down as atoms leak into the lattice. The behaviors indicated in Fig. 8-5 represent the so-called A-, B-, and C-type kinetics (Ref. 10). Polycrystalline film diffusion phenomena have been studied in the B to C range for the most part. Excellent reviews of

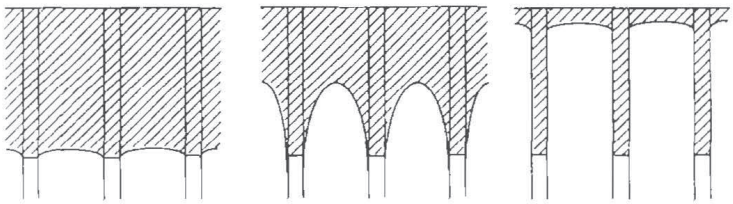


Figure 8-5. Schematic representation of type A (highest-temperature), B, and C (lowest-temperature) diffusion kinetics. (From Ref. 10).

the mathematical theories of GB diffusion including discussions of transport in these different temperature regimes, and applications to thin-film data are available (Refs. 11, 12). The best general source of this information is the volume *Thin Films—Interdiffusion and Reactions*, edited by Poate, Tu, and Mayer (Ref. 12) which also serves as an authoritative reference for much of the material discussed in this chapter. This book also contains a wealth of experimental mass transport data in thin-film systems.

The experimental measurements of the penetration of radioactive ^{195}Au into epitaxial (Fig. 8-6a) and polycrystalline (Fig. 8-6b) Au films provide a test of the above theories. They also importantly illustrate how the spectrum of diffusion behavior can be decomposed into the individual component mechanisms through judicious choice of film temperature and grain size. These data were obtained by incrementally sputter-sectioning the film, collecting the removed material in each section, and then counting its activity level. Very low

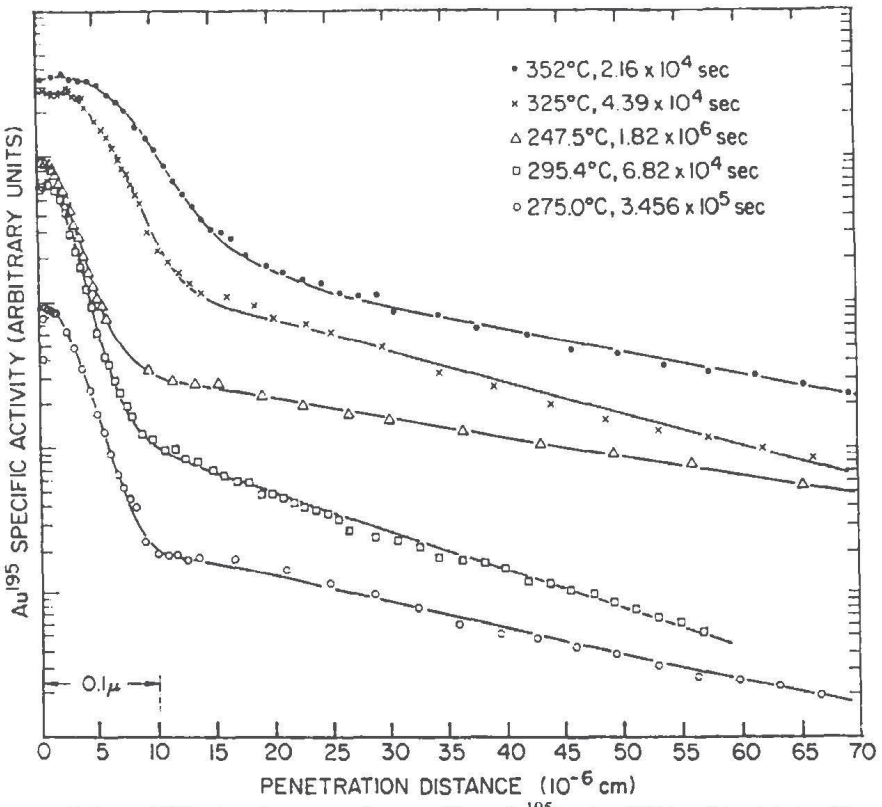


Figure 8-6a. Diffusional penetration profiles of ^{195}Au in (001) epitiaxial Au films at indicated temperatures and times. Lattice and dislocation diffusion dominate. (From Ref. 13).

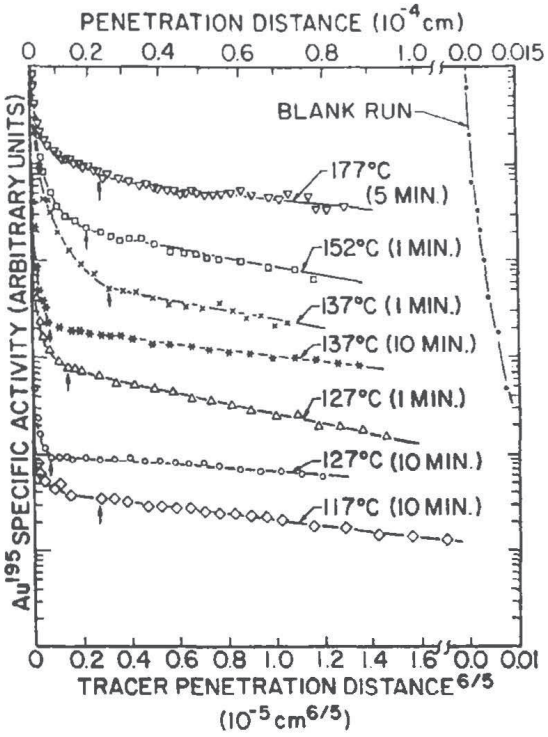


Figure 8-6b. Diffusional penetration profiles of ^{195}Au in polycrystalline films at indicated temperatures and times. Only GB diffusion is evident. (Reprinted with permission from Elsevier Sequoia, S.A., From D. Gupta and K. W. Asai, *Thin Solid Films* **22**, 121, 1974).

concentration levels can be detected because radiation-counting equipment is quite sensitive and highly selective. This makes it possible to measure shallow profiles and detect penetration at very low temperatures. The epitaxial film data display Gaussian-type lattice diffusion for the first 1000 to 1500 Å, followed by a transition to apparent dislocation short-circuit transport beyond this depth. Rather than high-angle boundaries, these films contained a density of some 10^{10} to 10^{11} dissociated dislocations per cm^2. On the other hand, extensive low-temperature GB penetration is evident in fig. 8-6b without much lattice diffusion. The large differences in diffusional penetration between these two sets of data, which are consistent with the systematics illustrated in Fig. 8-2, should be noted. For epitaxial Au a mixture of lattice and dislocation diffusion is expected for $\rho_d \approx 10^{10}/\text{cm}^2$ at temperatures of $\sim 0.4T_M$. Only GB diffusion is expected, however, at temperatures of $\sim 0.3T_M$ for a grain size of 5×10^{-5} cm, and this is precisely what was observed.

8.2.3. Diffusion in Miscible and Compound-Forming Systems

8.2.3.1. Miscible Systems. It is helpful to initiate the discussion on diffusion in miscible systems by excluding the complicating effects of grain boundaries. Bulk materials contain large enough grains so that the influence of GBs is frequently minimal. For thin films a couple where both layers are single crystals (e.g., a heteroepitaxial system) must be imagined. Under such conditions, the well-established macroscopic diffusion analyses hold. Upon interdiffusion in miscible systems, there is no crystallographic change, for this would imply new phases. Rather, each composition will be accessed at some point or depth within the film as a continuous range of solid solutions is formed. When the intrinsic atomic diffusivities are equal, i.e., $D_A = D_B$, the profile is symmetric and Eq. 1-27a governs the resultant diffusion. On the other hand, it is more common that $D_A \neq D_B$, so A and B atoms actually migrate with unequal velocities because they exchange with vacancies at different rates.

As an example of a miscible system, consider the much-studied Au–Pd polycrystalline thin-film couple in Fig. 8-7 (Ref. 15). Both AES sputter sectioning and RBS methods were employed to obtain the indicated profiles, whose apparent symmetry probably reflects the lack of a strong diffusivity dependence on concentration. It is very tempting to analyze these data by fitting them to an error-function-type solution. Effective diffusivity values could be obtained, but they would tend to have limited applicability because of the heterogeneous character of the film matrix. It must not be forgotten that

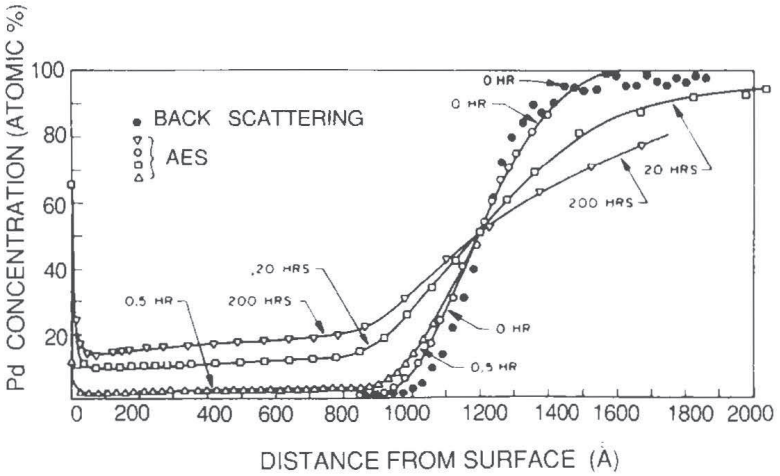


Figure 8-7. Palladium concentration profiles in a Au–Pd thin-film diffusion couple measured by RBS and AES techniques. (Reprinted with permission from Elsevier Sequoia, S.A., from P. M. Hall, J. M. Morabito and J. M. Poate, *Thin Solid Films* **33**, 107, 1976).

GB diffusion is the dominant mechanism in this couple. Therefore, the appropriate GB analysis is required in order to extract fundamental transport parameters. With this approach, it was found that a defect-enhanced admixture of GB and lattice diffusion was probably responsible for the large changes in the overall composition of the original films. Diffusional activation energies obtained for this film system are typically 0.4 times that for bulk diffusion, in accord with the systematics for GB diffusion.

8.2.3.2. Compound-Forming Systems. Many of the interesting binary combinations employed in thin-film technology react to form compounds. Since the usual configuration is a planar composite structure composed of elemental films on a flat substrate, layered compound growth occurs. The concentration–position profile in such systems is schematically indicated in Fig. 8-8. Each of the terminal phases is assumed to be in equilibrium with the intermediate compound. The compound shown is stable over a narrow rather than broad concentration range. Both types of compound stoichiometries are observed to form. With time, the compound thickens as it consumes the α phase at one interface and the β phase at the other interface.

It is instructive to begin with the simplified analysis of the kinetics of compound growth based on Fig. 8-8. Only the γ phase (compound) interface in equilibrium with α is considered. Since A atoms lost from α are incorporated into γ, the shaded areas shown are equal. With respect to the interface

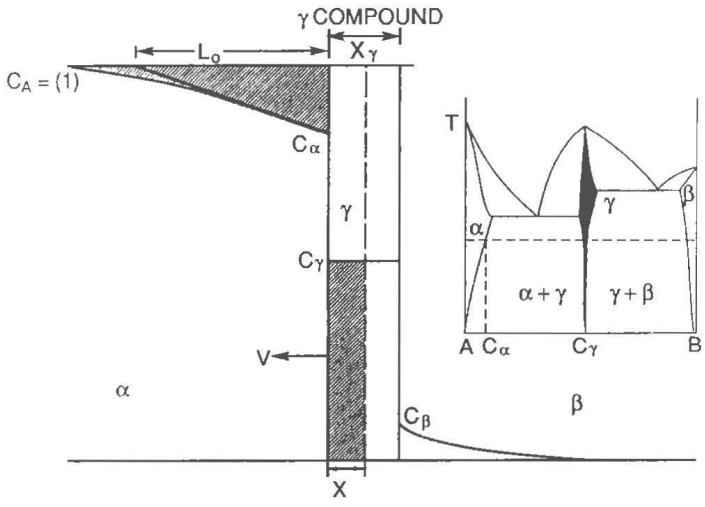


Figure 8-8. Depiction of intermediate compound formation in an A–B diffusion couple. Reaction temperature is dotted in on phase diagram.

moving with velocity V, the following mass fluxes of A must be considered:

$$\text{flux into interface} = C_\alpha V - D_\alpha \left(\frac{dC_\alpha}{dx} \right)_{\text{int}}.$$

$$\text{flux away from interface} = C_\gamma V.$$

These fluxes remain balanced for all times, so by equating them we have

$$V = \frac{dX}{dt} = \frac{D_\alpha (dC_\alpha / dx)}{C_\alpha - C_\gamma}, \tag{8-8}$$

where X is the compound layer thickness. From the simple geometric construction shown, dC_α / dx can be approximated by $(C_A - C_\alpha)/L_0$. Therefore as growth proceeds, L_0 increases while V decreases. If the shaded area within the α phase can be approximated by $(1/2)L_0(C_A - C_\alpha)$, and this is set equal to $C_\gamma X$, then $L_0 = 2C_\gamma X/(C_A - C_\alpha)$. Substituting for dC_α / dx in Eq. 8-8 leads to

$$\frac{dX}{dt} = \frac{D_\alpha}{2X} \frac{(C_A - C_\alpha)^2}{(C_\alpha - C_\gamma)C_\gamma}. \tag{8-9}$$

Upon integrating, the α-γ portion of the compound layer thickness is obtained as

$$X = \frac{\left[D_\alpha (C_A - C_\alpha)^2 \right]^{1/2} t^{1/2}}{\left[(C_\alpha - C_\gamma) C_\gamma \right]^{1/2}}. \tag{8-10}$$

A similar expression holds for the β–γ interface, and both solutions can be added together to yield the final compound layer thickness X_γ; i.e.,

$$X_\gamma = \text{const } t^{1/2}. \tag{8-11}$$

The important feature to note is that parabolic growth kinetics is predicted. Thermally activated growth is also anticipated, but with an effective activation energy dependent on an admixture of diffusion parameters from both α and β phases.

Among the important and extensively studied thin-film compound-forming systems are Al–Au (used in interconnection/contact metallurgy) and metal–silicon (used as contacts to Si and SiO_2); they will be treated later in the chapter. Parabolic growth kinetics is almost always observed in these systems. When diffusion is sufficiently rapid; however, growth may be limited by the speed of interfacial reaction. Linear kinetics varying simply as t then ensue,

but only for short times. For longer times linear growth gives way to diffusion-controlled parabolic growth.

8.2.4. The Kirkendall Effect

The Kirkendall effect has served to illuminate a number of issues concerning solid-state diffusion. One of its great successes is the unambiguous identification of vacancy motion as the operative atomic transport mechanism during interdiffusion in binary alloy systems. The Kirkendall experiment requires a diffusion couple with small inert markers located within the diffusion zone between the two involved migrating atomic species. An illustration of what happens to the marker during thin-film silicide formation is shown in Fig. 8-9. Assuming that metal (M) atoms exchange sites more readily with vacancies than do Si atoms, more M than Si atoms will sweep past the marker. In effect, more of the lattice will move toward the left! To avoid lattice stress or void generation, the marker responds by shifting as a whole toward the right. The reverse is true if Si is the dominant migrating specie. Such marker motion has indeed been observed in an elegant experiment (Ref. 16) employing RBS methods to analyze the reaction between a thin Ni film and a Si wafer. Implanted Xe, which served as the inert maker, moved toward the surface of

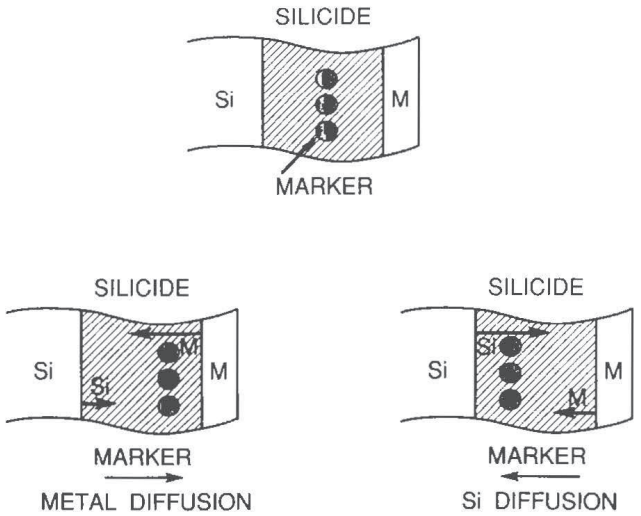


Figure 8-9. Schematic of Kirkendall marker motion during silicide formation. (Reprinted with permission from John Wiley and Sons, from J. M. Poate, K. N. Tu and J. W. Mayer, eds., *Thin Films: Interdiffusion and Reactions*, Copyright © 1978, John Wiley and Sons).

the couple during formation of Ni_2Si. The interpretation, therefore, is that Ni is the dominant diffusing specie.

8.2.5. Diffusion Size Effects (Ref. 17)

A linear theory of diffusion has been utilized to describe the various transport effects we have considered to this point and, except for this section, will be assumed for the remainder of the thin-film applications in this book. The macroscopic Fick diffusion equations defined by Eqs. 1-21 and 1-24 suffice as an operating definition of what is meant by linear diffusion theory. There are, however, nonlinear diffusion effects that may arise in thin-film structures when relatively large composition changes occur over very small distances (e.g., superlattices). To understand nonlinear effects, we reconsider atomic diffusion between neighboring planes in the presence of a free-energy gradient driving force. As a convenient starting point, two pertinent equations (1-33 and 1-35) describing this motion are reproduced here:

$$r_N = 2\nu \exp - \frac{G_D}{RT} \sinh \frac{\Delta G}{RT}, \tag{8-12}$$

$$v = DF/RT. \tag{8-13}$$

An expansion of $\sinh(\Delta G/RT)$ yields

$$\sinh \frac{\Delta G}{RT} = \frac{\Delta G}{RT} + \frac{1}{3!}\left(\frac{\Delta G}{RT}\right)^3 + \frac{1}{5!}\left(\frac{\Delta G}{RT}\right)^5 + \cdots. \tag{8-14}$$

Under conditions where $\Delta G/RT < 1$, the higher-order terms are small compared with the first, which is the source of the linear effects expressed by the Nernst–Einstein equation. Linear behavior is common because the lattice cannot normally support large energy gradients.

Now consider nonideal concentrated alloys where the free energies per atom or chemical potentials, μ_i, at nearby planes 1 and 2 are defined by (Eq. 1-9)

$$\mu_1 = \mu^\circ + kT \ln a_1 = \mu^\circ + kT \ln \gamma_1 C_1,$$

$$\mu_2 = \mu^\circ + kT \ln a_2 = \mu^\circ + kT \ln \gamma_2 C_2. \tag{8-15}$$

Here $\mu = G/N_A$, N_A is Avogadro's number, the activity a is defined by the product of the activity coefficient γ and concentration C, and μ° is the chemical potential of the specie in the standard state. The force on an atom (f) is defined by the negative spatial derivative of μ:

$$f = -\frac{d\mu}{dx} \approx \frac{\mu_2 - \mu_1}{N_l a_0},$$

and the force on a mole of atoms is

$$F = N_A f.$$

If F is also defined as $2\,\Delta G/a_0$ (Eq. 1-35), then

$$\frac{\Delta G}{RT} = \frac{a_0 F}{2RT} = \frac{\ln(\gamma_2 C_2/\gamma_1 C_1)}{2N_l}, \tag{8-16}$$

where N_l is the number of lattice spacings (a_0) included between planes 1 and 2. The ratio $\gamma_2 C_2/\gamma_1 C_1$ typically ranges from 10 to 10^3. In conventional thin films, $N_l > 100$, so $\Delta G/RT$ is small compared with unity. Only the first term in the expansion of $\sinh(\Delta G/RT)$ need be retained, which, as noted earlier, defines diffusion in the linear range.

Imagine now what happens when N_l is about 5 to 10 so that film dimensions of only 10–20 Å are involved. At the highest values of $\gamma_2 C_2/\gamma_1 C_1$, the quantity $\Delta G/RT$ is approximately unity. The higher-order terms in Eq. 8-14 can no longer be neglected now, and this leads to the nonlinear region of chemical diffusion. If only the cubic term is retained, a combination of Eqs. 8-12 to 8-14 and 1-33 to 1-34 yields

$$v = \frac{D}{RT}\left(F + \frac{a_0^2 F^3}{24(RT)^2}\right) \tag{8-17}$$

rather than the Nernst–Einstein relation. For an ideal solution, $\mu = kT \ln C$, and therefore $f = (-kT/C)(dC/dx)$. The macroscopic mass flux J is given by the product of atomic concentration and velocity, and accordingly

$$J = Cv = -D\frac{dC}{dx} - \frac{Da_0^2}{24C^2}\left(\frac{dC}{dx}\right)^3. \tag{8-18}$$

The first term is the readily recognizable Fickian flux, which is the source of linear diffusion effects. By taking the negative divergence of the flux (Eqs. 1-23 and 1-24), we obtain

$$\frac{\partial C}{\partial t} = D\frac{\partial^2 C}{\partial x^2} + \frac{Da_0^2}{8C^2}\left(\frac{dC}{dx}\right)^2\frac{\partial^2 C}{\partial x^2}. \tag{8-19}$$

This fifth-degree nonlinear differential equation was developed by Tu (Ref. 17), who termed it the "kinetic nonlinear" equation. It should not be confused with a similar "thermodynamic nonlinear" equation containing a $\partial^4 C/\partial x^4$ term used to describe diffusion in compositionally modulated films of small layer thickness.

As a simple example illustrating diffusion size effects, consider a composite film structure with layers d thick. Initially, the solute concentration varies

sinusoidally above an average level C_0 as

$$C(x,0) = C_0 + C_i \sin(\pi x/d) \qquad (C_i = \text{constant}). \tag{8-20}$$

If the film layer is thick, linear diffusion is expected. The solution that satisfies the Fick diffusion equation under the given conditions is

$$C(x,t) = C_0 + C_i \sin\frac{\pi x}{d} \exp -\frac{\pi^2 Dt}{d^2}. \tag{8-21}$$

When heated, compositional gradients throughout the film structure are reduced through interdiffusion. A measure of the extent of homogenization is

$$\left(C(d/2,t) - C_0\right)/C_i = e^{-\pi^2 Dt/d^2}. \tag{8-22}$$

As the film thickness shrinks, homogenization occurs more rapidly since diffusion distances are reduced. On further size reduction, a point is reached where large free-energy gradients cause entrance into the regime of nonlinear diffusion. Now Eq. 8-19 applies, and the reader can easily show that Eq. 8-21 is no longer a solution. Initially, compositional smoothing will be governed by the nonlinear term, and the actual kinetics and spatial concentration distribution will therefore be rather complex. But after some homogenization, $\ln(\gamma_2 C_2/\gamma_1 C_1)$ diminishes to the point where the linear diffusion term dominates the interdiffusion. An exponential decay of the profile amplitude should then characterize the long-time kinetics.

8.3. Interdiffusion in Metal Alloy Films

8.3.1. Reactions at a Solder Joint

One of the best ways to appreciate the importance of interdiffusion effects in metal films is to consider the interfacial region between a fabricated Si chip and the solder joint that connects it to the outside world. This is shown in Fig. 8-10, and, following Tu (Ref. 17), we note that the two levels of Al metalization interconnections, which contact the Si devices above, must also be bonded to the solder ball below. Anyone who has tried to solder Al is acquainted with the difficulties involved. In this case, they are overcome by using an evaporated Cr–Cu–Au thin-film structure. Since the surface of Al is easily oxidized, it is difficult to solder with the Pb–Sn alloy, so a Cu layer is introduced. The intention is to utilize the fast Cu–Sn reaction to form intermetallic compounds. However, Cu adheres poorly to oxidized Al and SiO_2 surfaces. Moreover, when molten, the relatively massive Pb–Sn consumes the

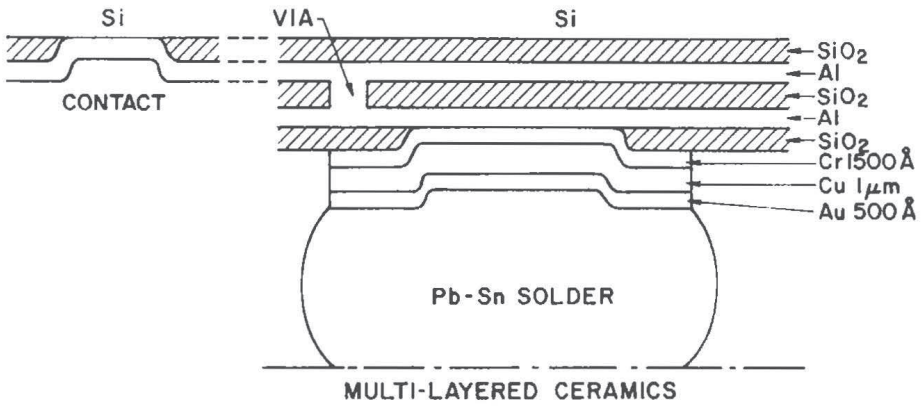


Figure 8-10. Schematic diagram of solder contact to Al by means of the trimetal Cr–Cu–Au film metallization scheme. (Reprinted with permission from Ref. 17).

Cu and then tends to dewet on the Al surface. Therefore, Cr is introduced as a glue layer between the Al and SiO_2 and to prevent the molten solder from dewetting. The Cu surface needs to be protected against atmospheric corrosion because corroded Cu surfaces do not solder well. Therefore, a thin film of Au is introduced to passivate the Cu surface. Since Au dissolves rapidly in Pb and Sn, a solder richer in Pb than the eutectic composition is used. This allows for enough Pb to dissolve Au and sufficient Sn to react with Cu. The reaction between the excess Pb and Cu is limited because these elements do not form extended solid solutions or intermetallic compounds. Thus, in order to fulfill the functions of adhesion, soldering, and passivation, this elaborate trimetal film structure is required.

There are additional solid-state diffusion effects between metal layers to contend with. At temperatures close to 200 °C, Cu can diffuse rapidly through GBs of Cr even though these metals are basically immiscible. When this happens, the interfacial adhesion at the Cr–SiO_2 interface is adversely affected. Moreover, Cu can diffuse outward through the Au in which it is miscible. At the Au surface it forms an oxide that interferes with soldering. This one method of joining (the flip-chip technology) has generated a host of mass-transport phenomena. For this reason, there has been considerable interest in thin-film interdiffusion studies of Cr–Cu, Au–Cu, and Cu–Sn systems. Other binary combinations from this group of involved elements, such as Al–Au and Al–Cu, have received even more attention. Miscible, immiscible, as well as compound-forming systems are represented. For the most part, vacancy diffusion is the accepted diffusion mechanism. However, in the case of the noble metals Cu and Au in the group IV matrices of Sn and Pb, anomalously rapid migration through interstitial sites is believed to occur.

8.3.2. GB Diffusion in Alloy Films

There have been a considerable number of fundamental interdiffusion studies in metal alloy films that have been interpreted in terms of GB transport models. In order to exclude the complicating effects of compounds and precipitates, the systems selected were primarily limited to those displaying solid solubility. Results from a representative group of investigations are entered in Table 8-1, where the diffusivities are expressed in terms of the pre-exponential factor (δD_b) and activation energy.

Two broad categories of experimental techniques were employed in gathering these data. Sputter sectioning through the film is the basis of the first technique. In the commonly employed AES depth-profiling method, the film is analyzed continuously as it is simultaneously thinned by sputter etching. Profiles appear similar to those shown in Fig. 8-6a, b.

The second category is based on permeation and surface accumulation techniques. An example shown in Fig. 8-11a utilizes AES signal-sensing methods to detect Ag penetration through a Au film and subsequent spreading along the exit surface (Ref. 19). The signal reflects this by building slowly at first after an incubation period, then changing more rapidly and finally saturating at long times. Diffusivities are then unfolded by fitting data to an assumed kinetics (shown in Fig. 8-11a) of concentration buildup with time. When type C kinetics (Fig. 8-5) prevails, D_b values may be simply estimated by equating the film thickness to the GB diffusion length $\sim 2\sqrt{D_b t}$, where t

Table 8-1. Grain-Boundary Diffusion in Thin Metal Films

Diffusant	Matrix	δD_b (cm^3/sec)	E_b (eV)	Remarks
Al	Cu	5.1×10^{-7}	0.94	Polycrystalline films
^{195}Au	Au	9.0×10^{-10}	1.00	Polycrystalline films
^{195}Au	Au	1.9×10^{-10}	1.16	(100) epitaxial
Cu	Al	4.5×10^{-8}	1.00	Polycrystalline
		1.8×10^{-10}	0.87	films
Ag	Au	4.5×10^{-12}	1.20	(111) epitaxial
^{195}Au	Ni-0.5%Co	1.4×10^{-10}	1.60	Polycrystalline films
Sn	Pb	6.9×10^{-10}	0.62	Polycrystalline films
Cr	Au	5.0×10^{-11}	1.09	Textured film
Ag	Cu	1.5×10^{-13}	0.75	Polycrystalline films
Pt	Cr	5.0×10^{-10}	1.69	Polycrystalline films
Cu	Al-0.2%Co	2.0×10^{-7}	0.56	Polycrystalline films
Ag	Au	5.0×10^{-14}	1.10	(100) epitaxial
^{119}Sn	Sn	5.0×10^{-8}	0.42	Polycrystalline films

From Ref. 18.

is the time required for the AES signal to appear. Interestingly, a grain-boundary Kirkendall effect shown in Fig. 8-11b has been suggested to account for the unequal GB diffusion rates of Ag and Au.

The high sensitivity inherent in detecting a signal rise from the low background enables very small atomic fluxes to be measured. This makes it possible to monitor transport at quite low temperatures. On the other hand, disadvantages include the electron-beam heating of films during measurement, and the need to maintain ultrahigh vacuum conditions because of the sensitivity of surface diffusion to ambient contamination.

Results for the sectioning methods suggest two GB diffusion regimes:

1. $D_b = 0.3 \exp - 7.5T_M/T$ cm^2/sec for large-angle boundaries where $E_b = 0.5E_L$.
2. $D_b = 2 \exp - 12.5T_M/T$ cm^2/sec for epitaxial films containing subboundaries or dissociated dislocations where $E_b = 0.7E_L$.

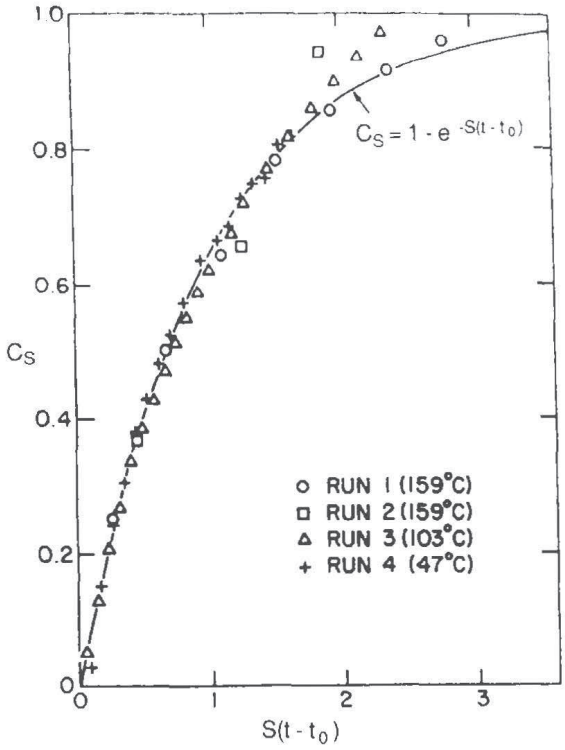


Figure 8-11a. Accumulation (C_s) of Ag on Au film surfaces as a function of normalized (reduced) time for different diffusional annealing temperatures. Constants S and t_0 (incubation time) depend on the run involved. (From Ref. 19).

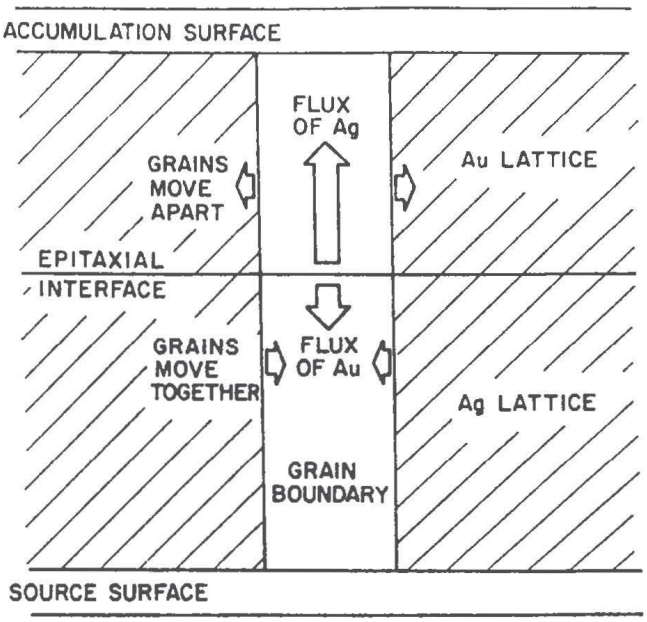


Figure 8-11b. Model of grain-boundary Kirkendall effect. (From Ref. 19).

For the permeation and surface accumulation methods, the activation energies appear to be somewhat lower. Data derived from these techniques are more susceptible to GB structure, since diffusant is transported through the most highly disordered boundaries first.

8.3.3. Formation of Intermetallic Compound Films

Perhaps the best-known example of intermetallic compound formation between metal films involves the interaction between Al and Au. For at least 20 years the combination of Al films and Au wires or balls served to satisfy bonding requirements in the semiconductor industry, but not without a significant number of reliability problems. When devices are heated to 250–300 °C for a few days, an Al–Au reaction proceeds to form a porous intermetallic phase around the Au ball bond accompanied by a lacy network of missing Al. One of the alloy phases, $AuAl_2$, is purple, which accounts for the appellation "purple plague." Even though the evidence is not definitive that the presence of $AuAl_2$ correlates with bond embrittlement, lack of strength, or degradation, formation of this compound is viewed with concern.

An extensive RBS study (Ref. 20) of compound formation in the Al–Au thin-film system is worth reviewing since it clarifies the role of film thickness,

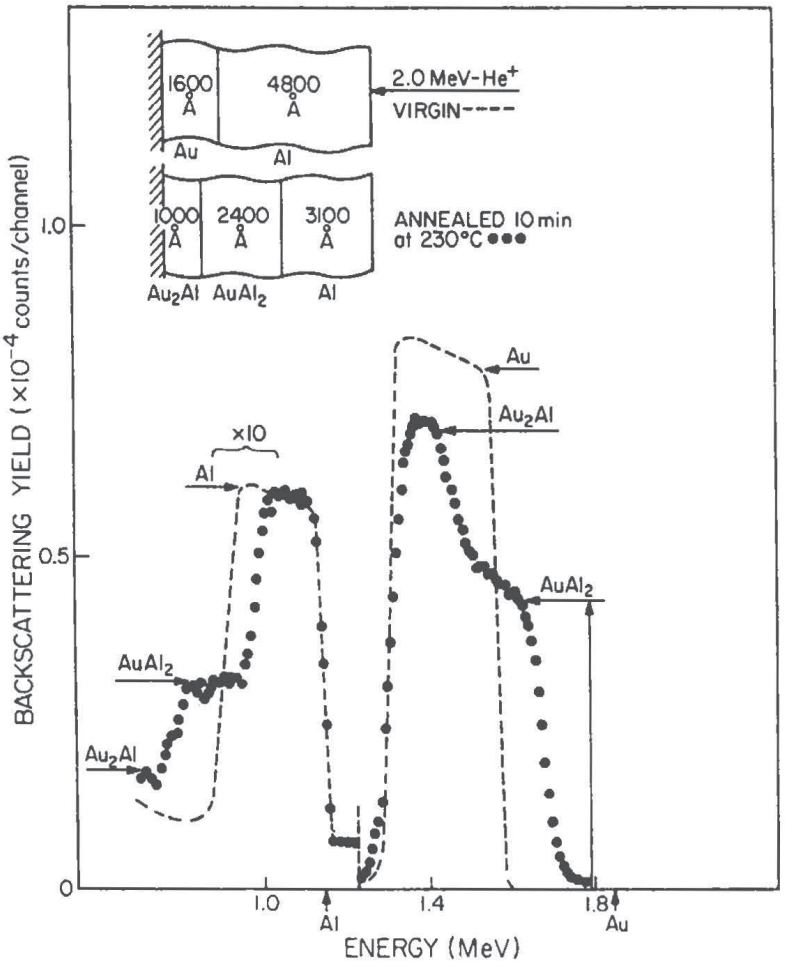


Figure 8-12. RBS spectrum showing formation of $AuAl_2$ and Au_2Al phases at 230 °C. (From Ref. 20).

temperature and time in influencing the reaction. Film couples with Al on top of Au were annealed, yielding RBS spectra such as shown in Fig. 8-12. Because there is such a large mass difference between Al and Au, there is no peak overlap despite the unfavorable spatial ordering of the metal layers. The stoichiometry of the peak shoulders in the annealed films corresponds to the compounds Au_2Al and $AuAl_2$, and the high-energy tail is indicative of Au transport through the Al film to the surface. From the fact that the $AuAl_2$ always appears at a higher energy than the Au_2Al, we know that it is closer to the air surface of the couple. By the methods outlined in Section 6.4.7, the compound thickness can be determined, and Fig. 8-13a reveals that both compounds grow with parabolic kinetics. The slopes of the compound thick-

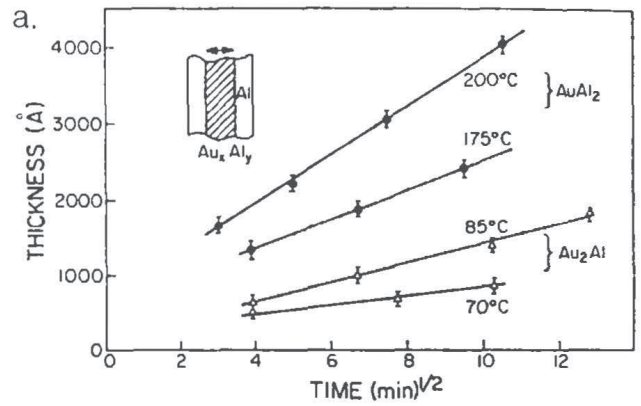


Figure 8-13a. Compound film thickness versus square root of time for $AuAl_2$ and Au_2Al at different annealing temperatures.

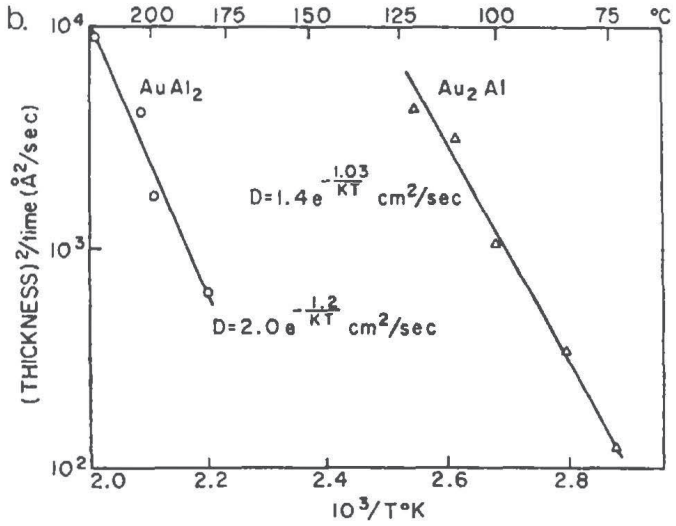


Figure 8-13b. Arrhenius plots for the kinetics of formation of $AuAl_2$ and Au_2Al compounds. (From Ref. 20).

ness–time$^{1/2}$ curves are proportional to the ubiquitous Boltzmann factor. Therefore, by plotting these slopes (actually the logs of the square of the slope in this case) versus $1/T$ K in the usual Arrhenius manner (Fig. 8-13b), we obtain activation energies for compound growth. The values of 1.03 and 1.2 eV can be roughly compared with the systematics given for FCC metals to elicit some clue as to the mass-transport mechanism for compound formation. Based on Au, these energies translate into equivalent Boltzmann factors of $\exp - 8.9T_M/T$ and $\exp - 10.4T_M/T$, respectively, suggesting a GB-assisted diffusion mechanism. Lastly, it is interesting to note how the sequence of

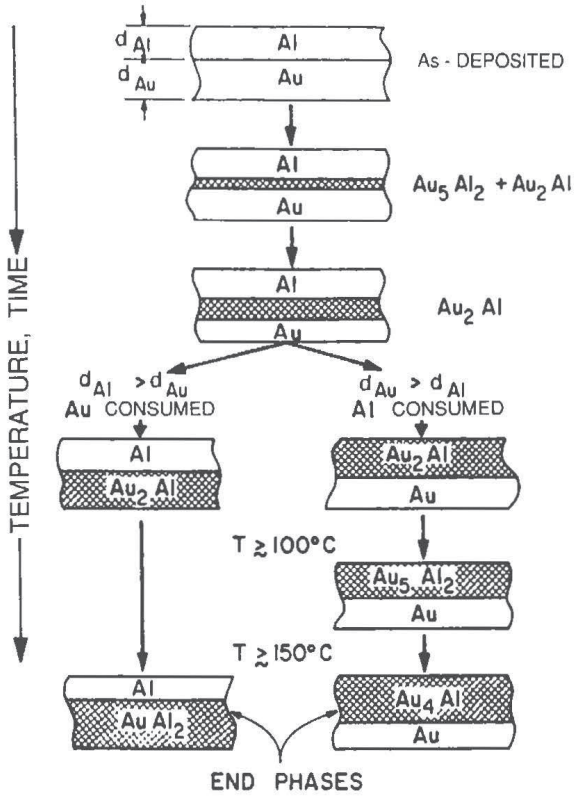
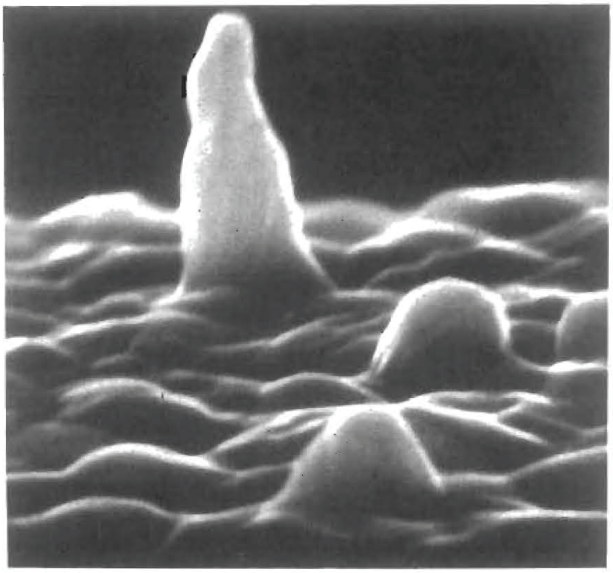


Figure 8-14. Schematic diagrams illustrating compound formation sequence in Al–Au thin film couples. End phases depend on whether $d_{Al} > d_{Au}$ or $d_{Au} > d_{Al}$.

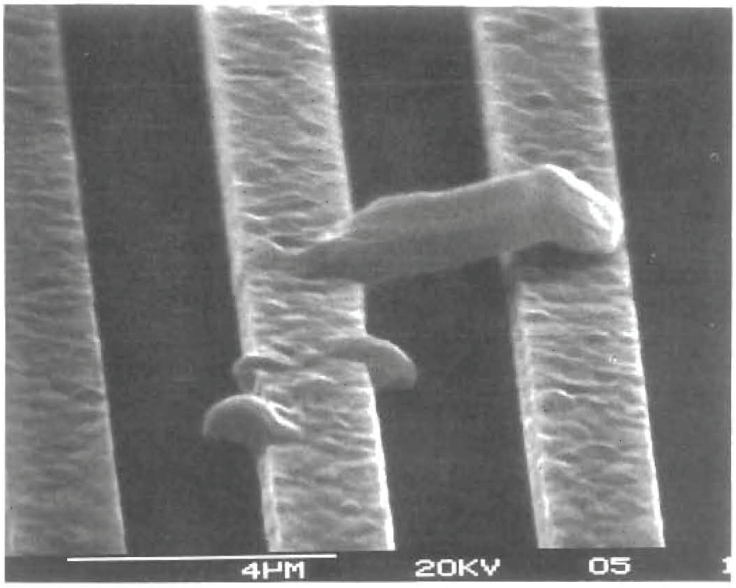
compound formation (Fig. 8-14) correlates with the equilibrium phase diagram (not shown). When the film thickness of Al exceeds that of Au, then the latter will be totally consumed, leaving excess Al. The observed equilibrium between Al and $AuAl_2$ layers is consistent with the phase diagram. Similarly, excess Au is predicted to finally equilibrate with the Au_4Al phase, as observed.

8.4. Electromigration in Thin Films

Electromigration, a phenomenon not unlike electrolysis, involves the migration of metal atoms along the length of metallic conductors carrying large direct current densities. It was observed in liquid metal alloys well over a century ago and is a mechanism responsible for failure of tungsten light-bulb filaments. Bulk metals approach the melting point when powered with current densities (J) of about 10^4 A/cm^2. On the other hand, thin films can tolerate densities of

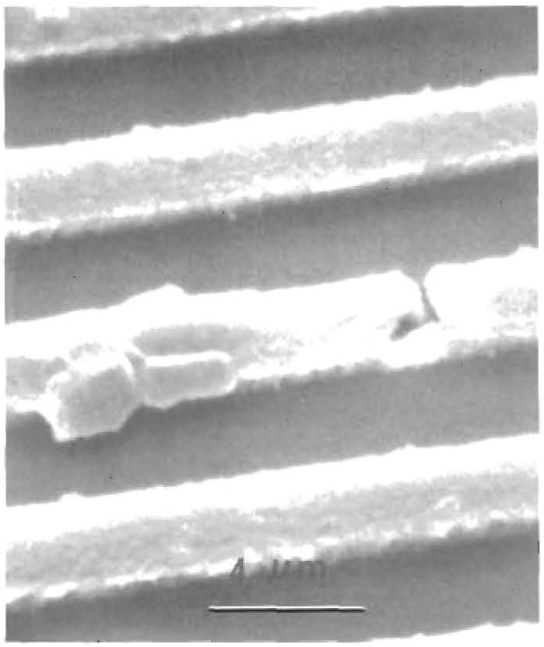


(a)



(b)

Figure 8-15. Manifestations of electromigration damage in Al films: (a) hillock growth, (from Ref. 21, courtesy of L. Berenbaum); (b) whisker bridging two conductors (courtesy of R. Knoell, AT & T Bell Laboratories); (c) nearby mass accumulation and depletion (courtesy S. Vaidya, AT & T Bell Laboratories).



(c)

Figure 8-15. *Continued.*

10^6 A/cm^2 without immediate melting or open-circuiting because the Joule heat is effectively conducted away by the substrate, which behaves as a massive heat sink. In a circuit chip containing some 100,000 devices, there is a total of several meters of polycrystalline Al alloy interconnect stripes that are typically less than 1.5 μm wide and 1 μm thick. Under powering, at high current densities, mass-transport effects are manifested by void formation, mass pileups and hillocks, cracked dielectric film overlayers, grain-boundary grooving, localized heating, and thinning along the conductor stripe and near contacts. Several examples of such film degradation processes are shown in Fig. 8-15. In bootstrap fashion the damage accelerates to the point where open-circuiting terminates the life of the conductor. It is for these reasons that electromigration has been recognized as a major reliability problem in integrated circuit metallizations for the past quarter century. Indeed, there is some truth to a corollary of one of Murphy's laws—"A million-dollar computer will protect a 25-cent fuse by blowing first." Analysis of the extensive accelerated testing that has been performed on interconnections has led to a general relationship between film mean time to failure (MTF) and J given by

$$\text{MTF}^{-1} = K(\exp - E_e/kT)J^n. \tag{8-23}$$

As with virtually all mass-transport-related reliability problems, damage is thermally activated. For Al conductors, n is typically 2 to 3, and E_e, the

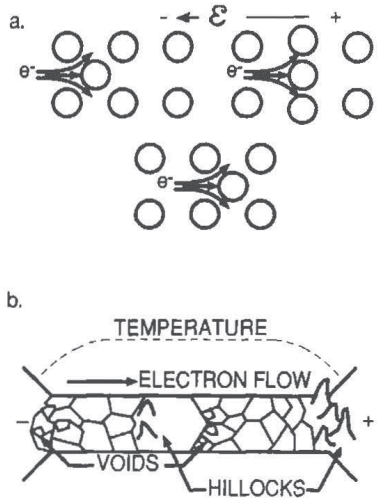


Figure 8-16. (a) Atomic model of electromigration involving electron momentum transfer to metal ion cores during current flow. (b) Model of electromigration damage in a powered film stripe. Mass flux divergences arise from nonuniform grain structure and temperature gradients.

activation energy for electromigration failure, ranges from 0.5 to 0.8 eV, depending on grain size. In contrast, an energy of 1.4 eV is associated with bulk lattice diffusion so that low-temperature electromigration in films is clearly dominated by GB transport. The constant K depends on film structure and processing. Current design rules recommend no more than 10^5 A/cm^2 for stripe widths of ~ 1.5 μm. Although Eq. 8-23 is useful in designing metalizations, it provides little insight into the atomistic processes involved.

The mechanism of the interaction between the current carriers and migrating atoms is not entirely understood, but it is generally accepted that electrons streaming through the conductor are continuously scattered by lattice defects. At high enough current densities, sufficient electron momentum is imparted to atoms to physically propel them into activated configurations and then toward the anode as shown in Fig. 8-16. This electron "wind" force is oppositely directed to and normally exceeds the well-shielded electrostatic force on atom cores arising from the applied electric field $\mathscr{E}$. Therefore, a net force F acts on the ions, given by

$$F = Z^* q \mathscr{E} = Z^* q \rho J, \tag{8-24}$$

where q is the electronic charge and $\mathscr{E}$ is, in turn, given by the product of the electrical resistivity of the metal, ρ, and J. An "effective" ion valence Z^* may be defined, and for electron conductors it is negative in sign with a magnitude usually measured to be far in excess of typical chemical valences.

On a macroscopic level, the observed mass-transport flux, J_m, for an element of concentration C is given by

$$J_m = Cv = CDZ^*q\rho J/RT, \tag{8-25}$$

where use has, once again, been made of the Nernst–Einstein relation. Electromigration is thus characterized at a fundamental level by the terms Z^* and D. Although considerable variation in Z^* exists, values of the activation energy for electrotransport in films usually reflect a grain-boundary diffusion mechanism.

Film damage is caused by a depletion or accumulation of atoms, which is defined by either a negative or positive value of dC/dt, respectively. By Eq. 1-23,

$$\frac{\partial C}{\partial t} = -\frac{\partial}{\partial x}\left(\frac{CDZ^*q\rho J}{RT}\right) - \frac{\partial}{\partial T}\left(\frac{CDZ^*q\rho J}{RT}\right)\frac{\partial T}{\partial x}. \tag{8-26}$$

The first term on the right-hand side reflects the isothermal, *structurally induced* mass flux divergence, and the second term represents mass transport in the presence of a *temperature gradient*. The resulting transport under these distinct conditions can be qualitatively understood with reference to Fig. 8-16b, assuming that atom migration is solely confined to GBs and directed toward the anode. Let us first consider electromigration under isothermal conditions. Because of varying grain size and orientation distributions, local mass flux divergences exist throughout the film. Each cross section of the stripe contains a lesser or greater number of effective GB transport channels. If more atoms enter a region such as a junction of grains than leave it, a mass pileup or growth can be expected. A void develops when the reverse is true. At highly heterogeneous sites where, for example, a single grain extends across the stripe width and abuts numerous smaller grains, the mass accumulations and depletions are exaggerated. For this reason, a uniform distribution of grain size is desirable. Of course, single-crystal films would make ideal interconnections because the source of damage sites is eliminated, but it is not practical to deposit them.

Electromigration frequently occurs in the presence of nonuniform temperature distributions that develop at various sites within device structures—e.g., at locations of poor film adhesion, in regions of different thermal conductivity, such as metal–semiconductor contacts or interconnect-dielectric crossovers, at nonuniformly covered steps, and at terminals of increased cross section. In addition to the influence of microstructure, there is the added complication of the temperature gradient. The resulting damage pattern can be understood by

considering the second term on the right-hand side of Eq. 8-26. For the polarity shown, all terms in parentheses are positive and $Cq\rho J/RT$ is roughly temperature independent, whereas DZ^* increases with temperature. Therefore, dC/dt varies as $-dT/dx$. Voids will thus form at the negative electrode, where $dT/dx > 0$, and hillocks will grow at the positive electrode, where $dT/dx < 0$. Physically, the drift velocity of atoms at the cathode increases as they experience a rising temperature. More atoms then exit the region than flow into it. At the anode the atoms decelerate in experiencing lower temperatures and thus pile up there. An analogy to this situation is a narrow strip of road leading into a wide highway (at the cathode). The bottleneck is relieved and the intercar spacing increases. If further down the highway it again narrows to a road, a new bottleneck reforms and cars will pile up (at the anode).

Despite considerable efforts to develop alternative interconnect materials, Al-base alloys are still universally employed in the industry. Their high conductivity, good adhesion, ease of deposition, etchability, and compatibility with other processing steps offset the disadvantages of being prone to corrosion and electromigration degradation. Nevertheless, attempts to improve the quality of Al metallizations have prompted the use of alternative deposition methods as well as the development of more electromigration-resistant alloys. With regard to the latter, it has been observed that Al alloyed with a few percent Cu can extend the electromigration life by perhaps an order of magnitude relative to pure Al. Reasons for this are not completely understood, but it appears that Cu reduces the GB migration of the solvent Al. The higher values for E_b which are observed are consistent with such an interpretation. Other schemes proposed for minimizing electromigration damage have included

1. Dielectric film encapsulation to suppress free surface growths
2. Incorporation of oxygen to generally strengthen the matrix through dispersion of deformation-resistant Al_2O_3 particles
3. Deposition of intervening thin metal layers in a sandwichlike structure that can shunt the Al in case it fails

The future may hold some surprises with respect to electromigration lifetime. Experimental results shown in Fig. 8-17 reveal reduction of film life as the linewidth decreases from 4 to 2 μm in accord with intuitive expectations. However, an encouraging increase in lifetime is surprisingly observed for submicron-wide stripes. The reason for this is the development of a bamboo-like grain structure generated in electron-beam evaporated films. Because the GBs are oriented normal to the current flow, the stripe effectively behaves as a single crystal. Similar benefits are not as pronounced in sputtered films.

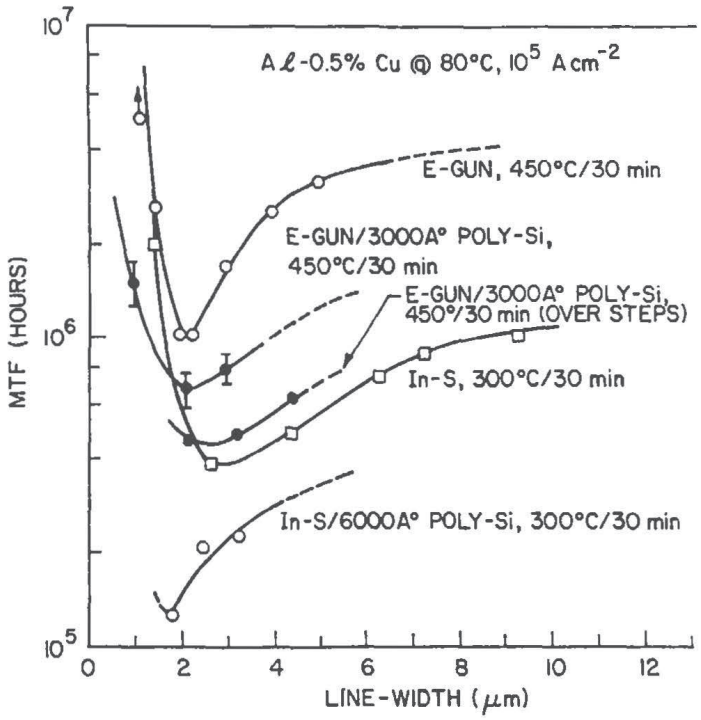


Figure 8-17. Mean time to failure as a function of stripe linewidth for evaporated (E-gun) and sputtered (S-gun, In–S) Al films. (From Ref. 22).

8.5. Metal - Semiconductor Reactions

8.5.1. Introduction to Contacts

All semiconductor devices and integrated circuits require contacts to connect them to other devices and components. When a metal contacts a semiconductor surface, two types of electrical behavior can be distinguished in response to an applied voltage. In the first type, the contact behaves like a P–N junction and rectifies current. The ohmic contact, on the other hand, passes current equally as a function of voltage polarity. In Section 10.4 the electrical properties of metal–semiconductor contacts will be treated in more detail.

Contact technology has dramatically evolved since the first practical semiconductor device, the point-contact rectifier, which employed a metal whisker that was physically pressed into the semiconductor surface. Today, deposited thin films of metals and metal compounds are used, and the choice is dictated by complex considerations; not the least of these is the problem of contact

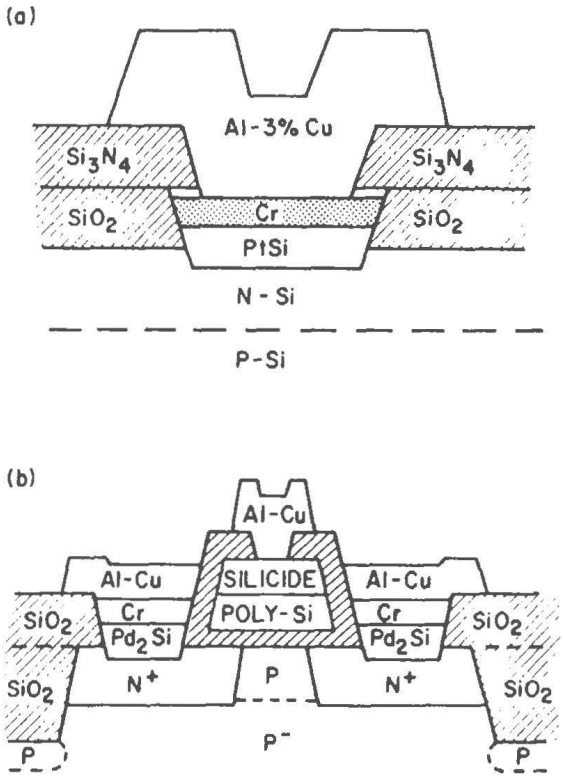


Figure 8-18. Schematic diagrams of silicide contacts in (a) bipolar and (b) MOS field effect transistor configurations. (Reprinted with permission from Ref. 17, © 1985 Annual Reviews Inc.).

instability during processing caused by mass-transport effects. For this reason, elaborate film structures are required to fulfill the electrical specifications and simultaneously defend against contact degradation. The extent of the problem can be appreciated with reference to Fig. 8-18, where both bipolar and MOS field effect transistors are schematically depicted. The operation of these devices need not concern us. What is of interest are the reasons for the Cr and metal silicide films that serve to electrically connect the Si below to the Al–Cu metal interconnections above. These bilayer structures have replaced the more obvious direct Al–Si contact, which, however, continues to be used in other applications. Contact reactions between Al and Si are interesting metallurgically and provide a good pedagogical vehicle for applying previously developed concepts of mass transport. A discussion of this follows. Means of minimizing Al–Si reactions through intervening metal silicide and diffusion-barrier films will then be reviewed.

8.5.2. Al - Si Reactions

Nature has endowed us with two remarkable elements: Al and Si. Together with oxygen, they are the most abundant elements on earth. It was their destiny to be brought together in the minutest of quantities to make the computer age possible. Individually, each element is uniquely suited to perform its intended function in a device, but together they combine to form unstable contacts. In addition to creating either a rectifying barrier or ohmic contact, they form a diffusion couple where the extent of reaction is determined by the phase diagram and mass-transport kinetics. The processing of deposited Al films for contacts typically includes a 400 °C heat treatment. This enables the Al to reduce the very thin native insulating SiO_2 film and "sinter" to Si, thereby lowering the contact resistance. Reference to the Al–Si phase diagram (Fig. 1-13) shows that at this temperature Si dissolves in Al to the extent of about 0.3 wt%. During sintering, Si from the substrate diffuses into the Al via GB paths in order to satisfy the solubility requirement. Simultaneously, Al migrates into the Si by diffusion in the opposite direction. As shown by the sequence of events in Fig. 8-19, local diffusion couples are first activated at several sites within the contact area. When enough Al penetrates at one point, the underlying P–N junction is shorted by a conducting metal filament, and junction "spiking" or "spearing" is said to occur.

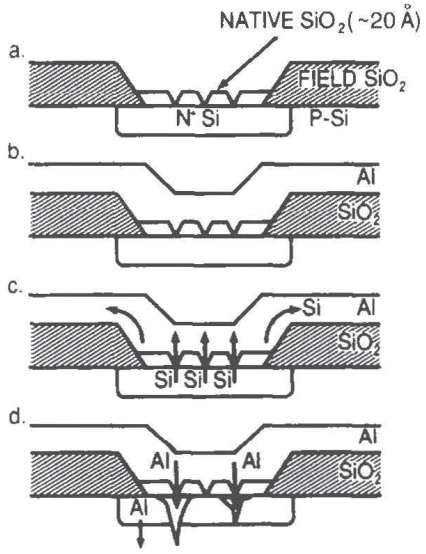


Figure 8-19. Schematic sequence of Al–Si interdiffusion reactions leading to junction spiking.

The remedy for the problem seems simple enough. By presaturating the Al with Si the driving force for interdiffusion disappears. Usually a 1 wt% Si–Al alloy film is sputtered for this purpose. However, with processing another complication arises. During the heating and cooling cycle Si is first held in solid solution but then precipitates out into the GBs of the Al as the latter becomes supersaturated with Si at low temperatures. The irregularly shaped Si precipitate particles, saturated with Al, grow epitaxially on the Si substrate. Electrically these particles are P type and alter the intended electrical characteristics of the contact. Thus, despite ease in processing, Al contact metallurgy is too unreliable in the VLSI regime of very shallow junction depths. For this reason, noble metal silicides such as Pd–Si have largely replaced Al at contacts.

There is yet another example of Al–Si reaction that occurs in field effect transistors. In this case, however, the contact to the gate oxide (SiO_2), rather than to the semiconductor source and drain regions, is involved. Historically, Al films were first used as gate electrodes, but, as noted on p. 24, they tend to reduce SiO_2, which is undesirable. Other metals are also problematical

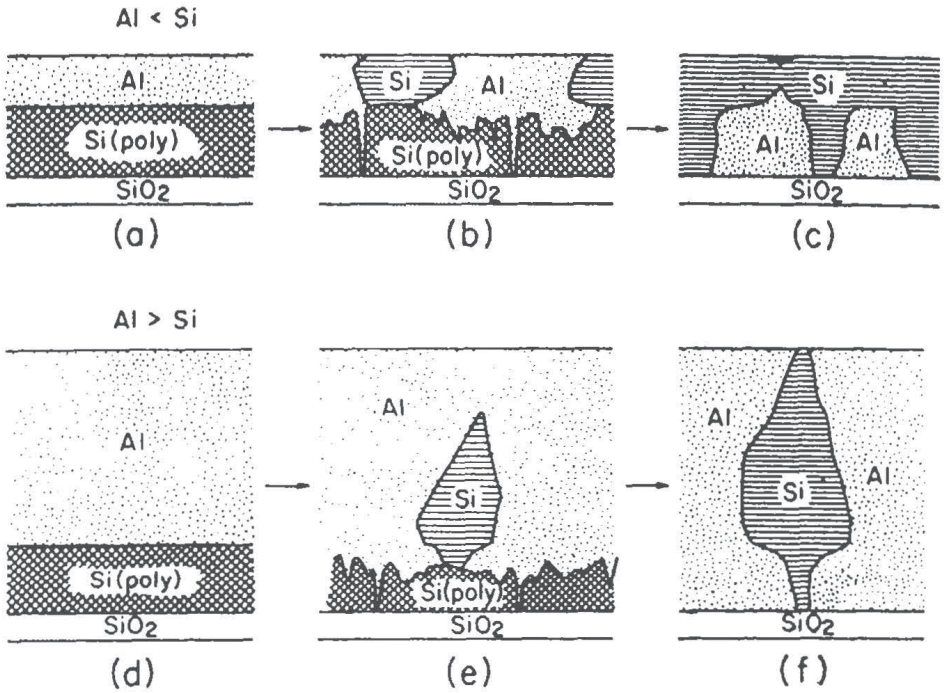


Figure 8-20. Depiction of reactions between Al and polysilicon films during annealing. Figures a, b, c refer to the case where $d_{Si} > d_{Al}$. Figures d, e, f refer to case where $d_{Al} > d_{Si}$. (From Ref. 23).

because of the potential reaction to form a silicide as well as oxide; an example is $3Ti + 2SiO_2 \rightarrow TiSi_2 + 2TiO_2$. For reliable device performance, the foregoing considerations have led to the adoption of poly-Si films as the gate electrode. Although there is now no driving force promoting reaction between Si and SiO_2, the chronic problem of Si–Al interdiffusion has re-emerged. The Al interconnections must still make contact to the gate electrode. To make matters worse, reaction of Al with poly Si is even more rapid than with single-crystal Si because of the presence of GBs. The dramatic alteration in the structure and composition in the Al–poly-Si–layered films following thermal treatment is shown schematically in Fig. 8-20. Reactions similar to those previously described for the Al–Si contact occur, and resultant changes are sensitive to the ratio of film thicknesses. It is easy to see why electrical properties would also be affected. Therefore, intervening silicide films and diffusion barriers must once again be relied on to separate Al from Si.

8.6. Silicides and Diffusion Barriers

8.6.1. Metal Silicides

In the course of developing silicides for use in contact applications, a great deal of fundamental research has been conducted on the reactions between thin metal films and single-crystal Si. Among the issues and questions addressed by these investigations are the following:

1. Which silicide compounds form?
2. What is the time and temperature dependence of metal silicide formation?
3. What atomic mass-transport mechanisms are operative during silicide formation? Which of the two diffusing species migrates more rapidly?
4. When the phase diagram indicates a number of different stable silicide compounds, which form preferentially and in what reaction sequence?

Virtually all thin-film characterization and measurement tools have been employed at one time or another in studying these aspects of silicide formation. In particular, RBS methods have probably played the major role in shaping our understanding of metal–silicon reactions by revealing compound stoichiometries, layer thicknesses, and the moving specie. Examples of the spectra obtained and their interpretation have been discussed previously. (See Section 6.4.7).

A summary of kinetic data obtained in silicide compounds formed with near-noble, transition, and refractory metals is contained in Table 8-2. This

Table 8-2. Silicide Formation

Silicide	Formation Temperature (°C)	Activation Energy (eV)	Growth Rate	Moving Specie	Formation Energy at 298 K (kcal/mole)
Au_2Si	100				
Co_2Si	350–500	1.5	$t^{1/2}$	Co	−27.6
Ni_2Si	200–350	1.5	$t^{1/2}$	Ni	−33.5
NiSi	350–700	1.4	t		−20.5
Pt_2Si	200–500	1.5	$t^{1/2}$	Pt	−20.7
PtSi	300	1.6	$t^{1/2}$		−15.8
FeSi	450–550	1.7	$t^{1/2}$	Si	−19.2
RhSi	350–425	1.95	$t^{1/2}$	Si	−16.2
HfSi	550–700	2.5	$t^{1/2}$	Si	−34
IrSi	400–500	1.9	$t^{1/2}$		−16.2
$CrSi_2$	450	1.7	t		−28.8
$MoSi_2$	525	3.2	t	Si	−31.4
WSi_2	650	3.0	$t, t^{1/2}$	Si	−22.2

From Refs. 12 and 24.

large body of work can be summarized in the following way:

Silicide	Formation Temp. (°C)	Growth Rate	Activation Energy (eV)
M_2Si	200	$t^{1/2}$	1.5
MSi	400	$t^{1/2}$	1.6–2.5
MSi_2	600	$t^{1/2}$	1.7–3.2

Three broad classes of silicides are observed to form: the metal-rich silicide (e.g., M_2Si), the monosilicide (MSi), and the silicon-rich silicide (e.g., MSi_2). As a rough rule of thumb, the formation temperature ranges from one third to one half the melting point (in K) of the corresponding silicide. Since fine-grained metal films are involved, it is not surprising that this rule is consistent with the GB diffusion regime. The activation energies roughly correlate with the melting point of the silicide, in agreement with general trends noted earlier.

In the metal-rich silicides, the metal is observed to be the dominant mobile specie, whereas in the mono- and disilicides Si is the diffusing specie. The crucial step in silicide formation requires the continual supply of Si atoms through the breaking of bonds in the substrate. In the case of disilicides, high temperatures are available to free the Si for reaction. At lower temperatures there is insufficient thermal energy to cause breaking of Si bonds, and the metal-rich silicides thus probably form by a different mechanism. It has been suggested that rapid interstitial migration of metal through the Si lattice assists bond breaking and thus controls the formation of such silicides.

The sequence of phase formation has only been established in a few silicide systems. Perhaps the most extensively studied of these is the Ni–Si system, for which the phase diagram and compound formation map are provided in Fig. 8-21. The map shows that Ni_2Si is always the first phase to form during low-temperature annealing. Clearly, Ni_2Si is not in thermodynamic equilibrium with either Ni or Si, according to the phase diagram. What happens next

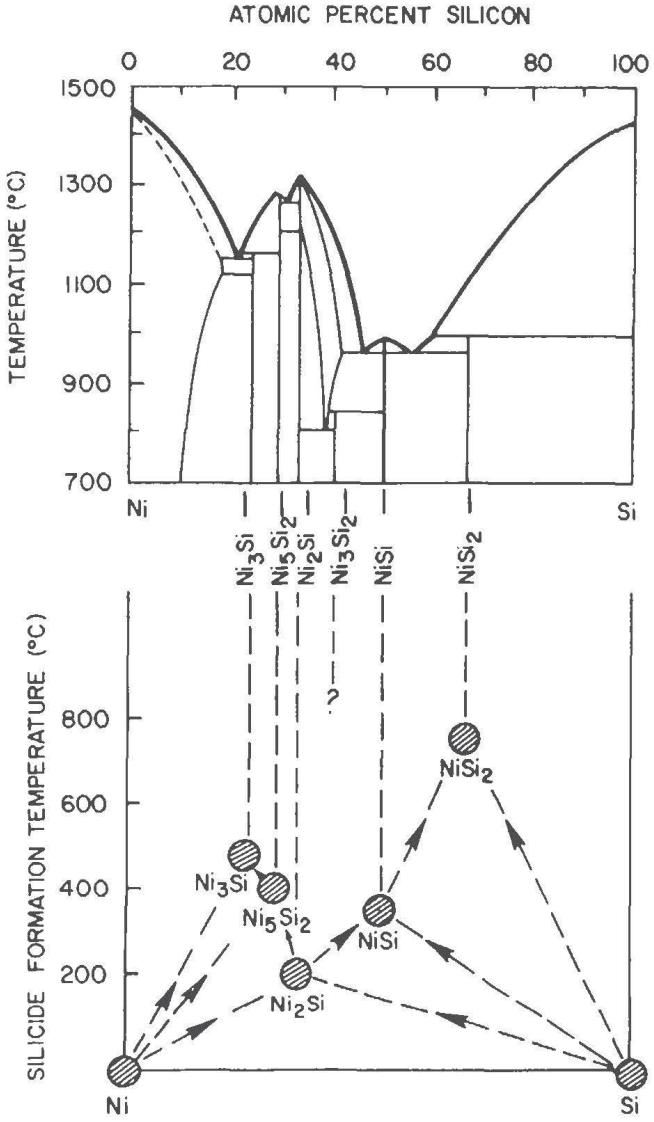


Figure 8-21. Map of thin-film Ni silicide formation sequence. Phase diagram of Ni–Si system shown on top. (Reprinted with permission from Ref. 17, © 1985 Annual Reviews Inc.).

depends on whether Si or Ni is present in excess. In the usual former case, where a Ni thin film is deposited on a massive Si wafer, the sequence proceeds first to NiSi and then to $NiSi_2$ at elevated temperatures. However, when a film of Si is deposited on a thicker Ni substrate, then the second and third compounds become Ni_5Si_2 and Ni_3Si. At elevated temperatures the resultant two-phase equilibrium (i.e., $Si-NiSi_2$ or $Ni-Ni_3Si$) conforms to the phase diagram. The question of the first silicide to form is a more complicated issue. It may be related to the ability to vapor-quench alloys to nucleate very thin, prior amorphous film layers. It is well known that bulk amorphous phases are readily formed by quenching metal-silicon eutectic melts. Therefore, it is suggested that silicide compounds located close to low-temperature eutectic compositions are the first to form.

Interestingly, in bulk diffusion couples all compounds appear to grow simultaneously at elevated temperatures. This does not seem to happen in films (at low temperature), but more sensitive analytical techniques may be required to clarify this issue.

8.6.2. Diffusion Barriers

Diffusion barriers are thin-film layers used to prevent two materials from coming into direct contact in order to avoid reactions between them. Paint and electrodeposited layers are everyday examples of practical barriers employed to protect the underlying materials from atmospheric attack. In a similar vein, diffusion barriers are used in thin-film metallization systems, and the discussion will be limited to these applications. We have already noted the use of silicides to prevent direct Al–Si contact. Ideally, a barrier layer X sandwiched between A and B should possess the following attributes (Ref. 25):

1. It should constitute a kinetic barrier to the traffic of A and B across it. In other words, the diffusivity of A and B in X should be small.
2. It should be thermodynamically stable with respect to A and B at the highest temperature of use. Further, the solubility of X in A and B should be small.
3. It should adhere well to and have low contact resistance with A and B and possess high electrical and thermal conductivity. Practical considerations also require low stress, ease of deposition, and compatibility with other processing.

Some of these requirements are difficult to achieve and even mutually exclusive so that it is necessary to make compromises.

A large number of materials have been investigated for use as barrier layers between silicon semiconductor devices and Al interconnections. These include

Table 8-3. Aluminum–Diffusion-Barrier–Silicon Contact Reactions

Diffusion Barrier	Reaction Temperature (°C)	Reaction Products	Failure Mechansims
Cr	300	Al_7Cr	C (E_C = 1.9 eV)
V	450	Al_3V, Al–V–Si	C (E_C = 1.7 eV)
Ti	400	Al_3Ti	C (E_C = 1.8 eV)
Ti–W	500		D
ZrN	550	Al–Zr–Si	C
PtSi	350	Al_2Pt, Si	C
Pd_2Si	400	Al_3Pd, Si	C
NiSi	400	Al_3Ni, Si	C
$CoSi_2$	400	Al_9Co_2, Si	C
$TiSi_2$	550	Al–Ti–Si	D
$MoSi_2$	535	$Al_{12}Mo$, Si	D
Ti–Pd_2Si	435	Al_3Ti	C
W–$CoSi_2$	500	$Al_{12}W$	C
TiN–PtSi	600	AlN, Al_3Ti	C
TiC–PtSi	600	Al_4C_3, Al_3Ti	C
TaN–NiSi	600	AlN, Al_3Ta	C

C = Compound formation; D = Diffusion
From Ref. 26.

silicides, refractory metals, transition metal alloys, transition metal compounds, as well as dual-layer barriers such as refractory metal–silicide, transition metal–silicide and transition metal compound–silicide combinations (Ref. 26). A compilation of these materials and reaction products is given in Table 8-3. Stringent physical requirements and the complexity of low-temperature interdiffusion and reactions have frequently necessitated the use of "diffusion barriers" to protect diffusion barriers. In order to gain a complete picture of the effectiveness of diffusion barriers, we need analytical techniques to reveal metallurgical interactions and their effect on the electrical properties of devices. For this reason, RBS measurements and, to a lesser extent, SIMS and AES depth profiling have been complemented by various methods for determining barrier heights (Φ_B) of contacts (Section 10.4). Changes in Φ_B are a sensitive indicator of low-temperature reactions at the metal–Si interface.

To appreciate the choice of barrier materials, we first distinguish among three models that have been proposed for successful diffusion-barrier behavior (Ref. 25).

1. Stuffed Barriers. Stuffed barriers rely on the segregation of impurities along otherwise rapid diffusion paths such as GBs to block further passage of

two-way atomic traffic there. The marked improvement of sputtered Mo and Ti–W alloys as diffusion barriers when they contain small quantities of intentionally added N or O impurities is apparently due to this mechanism. Impurity concentrations of $\sim 10^{-1}$ to 10^{-3} at% are typically required to decorate GBs and induce stuffed-barrier protection. In extending the electromigation life of Al, Cu may in effect "stuff" the conductor GBs.

*2. **Passive Compound Barriers.*** Ideal barrier behavior exhibiting chemical inertness and negligible mutual solubility and diffusivity is sometimes approximated by compounds. Although there are numerous possibilities among the carbides, nitrides, borides, and even the more conductive oxides, only the transition metal nitrides, such as TiN, have been extensively explored for device applications. TiN has proved effective in solar cells as a diffusion barrier between N–Si and Ti–Ag, but contact resistances are higher than desired in high-current-density circuits.

*3. **Sacrificial Barriers.*** A sacrificial barrier maintains the separation of A and B only for a limited duration. As shown in Fig. 8-22, sacrificial barriers exploit the fact that reactions between adjacent films in turn produce uniform layered compounds AX and BX that continue to be separated by a narrowing X barrier film. So long as X remains and compounds AX and BX possess adequate conductivity, this barrier is effective. The first recognized application of a sacrificial barrier involved Ti, which reacted with Si to form Ti_2Si and with Al to form $TiAl_3$. Judging from the many metal aluminide and occasional Al–metal–silicon compounds in Table 8-3, sacrificial barrier reactions appear to be quite common.

If the reaction rate kinetics of both compounds, i.e., AX, BX, are known, then either the effective lifetime or the minimum thickness of barrier required may be predicted. The following example is particularly instructive (Ref. 1). Suppose we consider a Ti diffusion barrier between Si and Al. Without imposition of Ti, the Al–Si combination is unstable. The question is, how

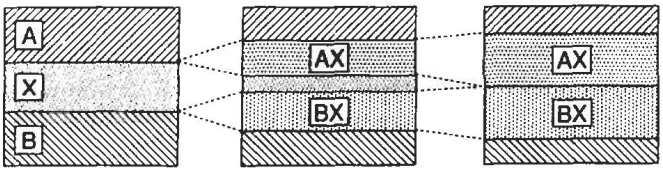


Figure 8-22. Model of sacrificial barrier behavior. A and B films react with barrier film X to form AX and BX compounds. Protection is afforded as long as X is not consumed. (Reprinted with permission from Elsevier Sequoia, S.A., from M.-A. Nicolet, *Thin Solid Films* **52**, 415, 1978).

much Ti should be deposited to withstand a thermal anneal at 500 °C for 15 min? At the Al interface, $TiAl_3$ forms with parabolic kinetics given by

$$d^2_{TiAl_3} = (1.5 \times 10^{15}) e^{-1.85\,eV/kT} t \ (\text{Å}^2), \tag{8-27}$$

where d_{TiAl_3} is the thickness of the $TiAl_3$ layer and t is the time in seconds. Similarly, the reaction of Ti with Si results in the formation of $TiSi_2$ with a kinetics governed by

$$d^2_{TiSi_2} = (5.74 \times 10^{9}) e^{-1.3\,eV/kT} t \ (\text{Å}^2). \tag{8-28}$$

For the specified annealing conditions, $d_{TiAl_3} = 1100$ Å and $d_{TiSi_2} = 130$ Å. An insignificant amount of Ti is consumed under ambient operating conditions. Therefore, the minimum thickness of Ti required is the sum of these two values, or 1230 Å.

In conclusion, we note that semiconductor contacts are thermodynamically unstable because they are not in a state of minimum free energy. The imposition of a diffusion barrier slows down the equilibration process, but the instability is never actually removed. Enhanced reliability is bought with diffusion barriers, but at the cost of increasing structural complexity and added processing expense.

8.7. Diffusion During Film Growth

We close the chapter by considering diffusion effects in films growing within a gas-phase ambient. In addition to the diffusional exchange between gas atoms and growing film, or the redistribution of atoms between film and substrate, there is the added complexity of transport across a moving boundary. Such effects are important in high-temperature oxidation of Si, one of the most-studied film growth processes. The resulting amorphous SiO_2 films find extensive use in microelectronic applications as an insulator, and as a mask used to pattern and expose some regions for processing while shielding other areas. In contrast to film deposition, where the atoms of the deposit originate totally from the vapor phase (as in CVD of SiO_2), oxidation relies on the reaction between Si and oxygen to sustain oxide film growth. This means that for every 1000 Å of SiO_2 growth, 440 Å (i.e., $1000\rho_{SiO_2}M_{Si}/\rho_{Si}M_{SiO_2}$) of Si substrate is consumed. The now-classic analysis of oxidation due to Grove (Ref. 27) has a simple elegance and yet accurately predicts the kinetics of thermal oxidation. In this treatment of the model, we assume a flow of gas

containing oxygen parallel to the plane of the Si surface. In order to form oxide at the Si–SiO_2 interface, the following sequential steps are assumed to occur:

1. Oxygen is transported from the bulk of the gas phase to the gas–oxide interface.
2. Oxygen diffuses through the growing solid oxide film of thickness d_0.
3. When oxygen reaches the Si–SiO_2 interface, it chemically reacts with Si and forms oxide.

The respective mass fluxes corresponding to these steps can be expressed by

$$J_1 = h_G(C_G - C_0), \tag{8-29}$$

$$J_2 = D(C_0 - C_i)/d_0, \tag{8-30}$$

$$J_3 = K_S C_i, \tag{8-31}$$

where the concentrations of oxygen in the bulk of the gas, at the gas–SiO_2 interface, and at the SiO_2–Si interface are respectively, C_G, C_0, and C_i. The quantities h_G, D, and K_S represent the gas mass-transport coefficient, the diffusion coefficient of oxygen in SiO_2, and the chemical reaction rate constant, respectively. Constants D and K_S display the usual Boltzmann behavior but with different activation energies, and h_G has a weak temperature dependence.

By assuming steady-state growth implying $J_1 = J_2 = J_3$, we easily solve for C_i and C_0 in terms of C_G:

$$C_0 = \frac{C_G(1 + K_S d_0/D)}{1 + K_S/h_G + K_S d_0/D}, \tag{8-32a}$$

$$C_i = \frac{C_G}{1 + K_S/h_G + K_S d_0/D}. \tag{8-32b}$$

Clearly, the grown SiO_2 has a well-fixed stoichiometry so that C_0 and C_i differ only slightly in magnitude, but sufficiently to establish the concentration gradient required for diffusion. In fact, $C_0 \approx C_i = C_G/(1 + K_S/h_G)$ in the so-called reaction-limited case where $D \gg K_S d_0$. Here, diffusion is assumed to be very rapid through the SiO_2, but the bottleneck for growth is the interfacial chemical reaction. On the other hand, under diffusion control, D is small so that $C_0 \approx C_G$ and $C_i \approx 0$. In this case the chemical reaction is sufficiently rapid, but the supply of oxygen is rate-limiting. The actual oxide growth rate is related to the flux, say J_3, and therefore the thickness of oxide at any time is expressed by

$$d(d_0)/dt = K_S C_i/N_0, \tag{8-33}$$

where N_0 is the number of oxidant molecules incorporated into a unit volume of film. For oxidation in dry O_2 gas, $N_0 = 2.2 \times 10^{22}$ cm^{-3}, whereas for steam (wet) oxidation $N_0 = 4.4 \times 10^{22}$ cm^{-3}, because half as much oxygen is contained per molecule.

Substitution of Eq. 8-32b into 8-33 and direct integration of the resulting differential equation yields

$$d_0^2 + Ad_0 = B(t + \tau), \tag{8-34}$$

where

$$A = 2D\left(\frac{1}{h_G} + \frac{1}{K_S}\right), \quad B = \frac{2DC_G}{N_0}, \quad \text{and} \quad \tau = \frac{d_i^2 + Ad_i}{B}.$$

The constant of integration τ arises only if there is an initial oxide film of thickness d_i present prior to oxidation, and therefore Eq. 8-34 is useful in describing sequential oxidations. A solution to this quadratic equation is

$$\frac{d_0}{A/2} = \sqrt{1 + \frac{t + \tau}{A^2/4B}} - 1, \tag{8-35}$$

from which the limiting long- as well as short-time growth kinetics relationships are easily shown to be

$$d_0^2 \approx Bt \qquad \text{for } t \gg A^2/4B, \tag{8-36}$$

$$d_0 \approx \frac{B}{A}(t + \tau) \qquad \text{for } t + \tau \ll \frac{A^2}{4B}. \tag{8-37}$$

The reader will recall similar parabolic and linear growth in metal compound and silicide films. All film growth is probably linear to begin with because parabolic growth implies an infinite initial thickening rate.

Values for the parabolic and linear rate constants for SiO_2, grown from (111) Si, are approximately (Ref. 28)

$$B = 186 \exp -\frac{0.71 \text{ eV}}{kT} \ \mu\text{m}^2/\text{hr} \qquad (\text{wet } O_2), \tag{8-38a}$$

$$B = 950 \exp -\frac{1.24 \text{ eV}}{kT} \ \mu\text{m}^2/\text{hr} \qquad (\text{dry } O_2), \tag{8-38b}$$

$$\frac{B}{A} = 7.31 \times 10^7 \exp -\frac{1.96 \text{ eV}}{kT} \ \mu\text{m/hr} \qquad (\text{wet } O_2), \tag{8-39a}$$

$$\frac{B}{A} = 5.89 \times 10^6 \exp -\frac{2.0 \text{ eV}}{kT} \ \mu\text{m/hr} \qquad (\text{dry } O_2), \tag{8-39b}$$

where all constants are normalized to 760 torr. Equations 8-36 and 8-37 serve as an aid in designing oxidation treatments. Different activation energies for B are obtained in wet and dry O_2 because the migrating species in each case is

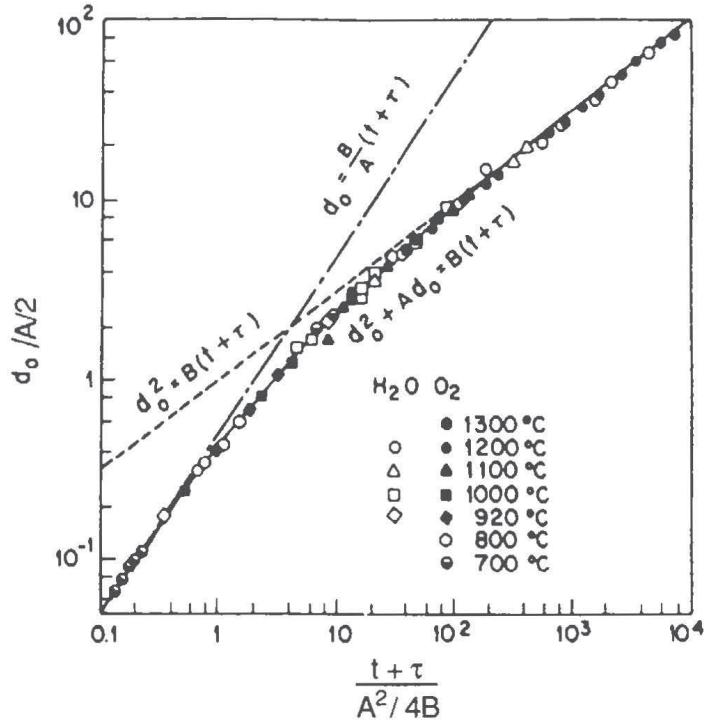


Figure 8-23. Oxidation kinetics behavior of Si in terms of dimensionless oxide thickness and time. The two limiting forms of the kinetics are shown. From A. S. Grove, *Physics and Technology of Semiconductor Devices*, Copyright © 1967, John Wiley and Sons. (Reprinted with permission.)

different, e.g., H_2O and OH as opposed to O_2 or O. However, the activation energy for B/A reflects the chemical reaction at the Si–SiO_2 interface and is the same regardless of the nature of the oxygen-bearing diffusant. A single dimensionless thickness–time plot shown in Fig. 8-23 very neatly summarizes Si oxidation behavior. The limiting linear and parabolic growth kinetics regimes are clearly identified.

Not all oxidation processes, however, display linear or parabolic growth kinetics. Some examples are presented in Chapter 12 in connection with protective oxide coatings.

EXERCISES

1. a. Establish generalized expressions for the lattice diffusivity as a function of temperature for semiconductors and alkali halides, using Fig. 5-6.

b. How does your expression for D_L compare with the diffusivity values for Si in Si (self-diffusion) in Fig. 8-3?

2. A P–N junction is produced by diffusing B from a continuous source ($C_0 = 10^{19}$ cm^{-3}) into an eptiaxial Si film with a background N level of 10^{15} cm^{-3}. Diffusion is carried out at 1100 °C for 30 min.

a. How far beneath the Si surface is the junction (i.e., where $C_N = C_P$). Use Eq. 1-27a.
b. If there is a 1% error in temperature, what is the percent change in junction depth?
c. By what percent will the junction depth change for a 1% change in diffusion time?

3. At what temperature will the number of Au atoms transported through grain boundaries equal that which diffuses through the lattice if the grain size is 2 μm? 20 μm?

4. The equation for transport of atoms down a single grain boundary where there is simultaneous diffusion into the adjoining grains is

$$\frac{\partial C_b}{\partial t} = D_b \frac{\partial^2 C_b}{\partial y^2} - \frac{2D_L}{\delta}\left(\frac{dC_L}{dx}\right)_{x=\delta/2}$$

Derive this equation by considering diffusional transport into and out of an element of grain boundary δ wide and dy long.

5. In the Pd–Au thin-film diffusion couple an approximate fit to the data of Fig. 8-7 can be made employing the equation

$$C(x, t) = \frac{C_0}{2}\operatorname{erfc}\frac{x}{2\sqrt{Dt}}.$$

a. Plot $C(x, t)$ vs. x.
b. From values of $dC/dx|_{x=0}$, estimate the values of D for the 0-h, 20-h, and 200-h data. Are these D values the same?
c. What accounts for the apparent interdiffusion between Au and Pd at 0 h?

6. a. Calculate the activation energy for dislocation pipe diffusion of Au in epitaxial Au films from the data of Fig. 8-6a.
b. Calculate the activation energy for grain-boundary diffusion of Au in polycrystalline Au films from the data of Fig. 8-6b.

In both cases make Arrhenius plots of the diffusivity data. Assume

$$D_L = 0.091 \exp - \frac{41.7 \text{ (kcal/mole)}}{RT} \text{ cm}^2/\text{sec}.$$

7. An N-type dopant from a continuous source of concentration C_0 is diffused into a P-type semiconductor film containing a single grain boundary oriented normal to the surface. If the background dopant level in the film is C_B, write an expression for the resulting P–N junction profile (y vs. x) after diffusion.

8. A 1-μm-thick film of Ni was deposited on a Si wafer. After a 1-h anneal at 300 °C, 600 Å of Ni_2Si formed.

a. Predict the thickness of Ni_2Si that would form if the Ni–Si couple were heated to 350 °C for 2 h.
b. In forming 600 Å of Ni_2Si, how much Si was consumed? [Note: The atomic density of Ni is 9×10^{22} atoms/cm^3.]
c. The lattice parameters of cubic Ni_2Si and Si are 5.406 Å and 5.431 Å, respectively. Comment on the probable nature of the compound–substrate interface.

9. The thermal stability of a thin-film superlattice consisting of an alternating stack of 100-Å-thick layers of epitaxial GaAs and AlAs is of concern.

a. If chemical homogenization of the layers is limited by the diffusion of Ga in GaAs, estimate how long it will take Ga to diffuse 50 Å at 25 °C?
b. *Roughly* estimate the temperature required to produce layers of composition $Ga_{0.75}Al_{0.25}As$–$Ga_{0.25}Al_{0.75}As$ after a 1-h anneal.

10. For electromigration in Al stripes assume $E_e = 0.7$ eV and $n = 2.5$ in Eq. 8-23. By what factor is MTF shortened (or extended) at 40 °C by

a. a change in E_e to 0.6 eV?
b. no change in E_e but a temperature increase to 85 °C?
c. a decrease in stripe thickness at a step from 1.0 to 0.75 μm?
d. an increase in current from 1 to 1.5 mA?

11. a. When there are simultaneous electromigration and diffusional fluxes of atoms, show that

$$\frac{\partial C}{\partial t} = D\frac{\partial^2 C}{\partial x^2} - v\frac{\partial C}{\partial x},$$

with v defined by Eq. 8-25.

b. For a diffusion couple ($C = C_0$ for $x < 0$ and $C = 0$ for $x > 0$) show that

$$C(x,t) = \frac{C_0}{2}\left[\exp\frac{vx}{D}\operatorname{erfc}\frac{x+vt}{\sqrt{4Dt}} + \operatorname{erfc}\frac{x-vt}{\sqrt{4Dt}}\right]$$

is a solution to the equation in part (a) and satisfies the boundary conditions.

c. A homogeneous Al film stripe is alloyed with a cross stripe of Cu creating two interfaces; (+) Al–Cu/Al and (−) Al/Al–Cu. Show, using the preceding solution, that the concentration profiles that develop at these interfaces obey the relation.

$$\ln\frac{C_+(x,t)}{C_-(x,t)} = \frac{vx}{D}.$$

12. The surface accumulation interdiffusion data of Fig. 8-11a can be fitted to the normalized equation $C_S = 1 - \exp - S(t - t_0)$. For

run 1: $S = 7.1 \times 10^{-1}\ \text{sec}^{-1}$,
run 2: $S = 1.4 \times 10^{-2}\ \text{sec}^{-1}$,
run 3: $S = 7.4 \times 10^{-4}\ \text{sec}^{-1}$,
run 4: $S = 2.6 \times 10^{-5}\ \text{sec}^{-1}$.

a. If S is thermally activated, i.e., $S = S_0\exp - E_S/kT$ (S_0 = constant), make an Arrhenius plot and determine the activation energy for diffusion of Ag in Au films.

b. What diffusion mechanism is suggested by the value of E_S?

13. a. Compare the time required to grow a 3500 Å thick SiO_2 film in dry as opposed to wet O_2 at 1100 °C. Assume the native oxide thickness is 30 Å.

b. A window in a 3500 Å SiO_2 film is opened down to the Si substrate in order to grow a gate oxide at 1000 °C for 30 minutes in dry O_2. Find the resulting thickness of both the gate and surrounding (field) oxide films.

REFERENCES

1. M.-A. Nicolet and M. Bartur, *J. Vac. Sci. Tech* **19**, 786 (1981).
2. R. W. Balluffi and J. M. Blakely, *Thin Solid Films* **25**, 363 (1975).
3. N. A. Gjostein, *Diffusion*, American Society for Metals, Metals Park, Ohio (1973).

4. J. C. C. Tsai, in *VLSI Technology*. 2nd ed., ed. S. M. Sze, McGraw-Hill, New York (1988).
5. S. M. Sze, *Semiconductor Devices–Physics and Technology*, Wiley, New York (1985).
6. D. C. Jacobson, *Ion-Beam Studies of Noble Metal Diffusion in Amorphous Silicon Layers*, Ph.D. Thesis, Stevens Institute of Technology (1989).
7. J. C. Fisher, *J. Appl. Phys.* **22**, 74 (1951).
8. R. T. Whipple, *Phil. Mag.* **45**, 1225 (1954).
9. T. Suzuoka, *Trans. Jap. Inst. Met.* **2**, 25 (1961).
10. L. G. Harrison, *Trans. Faraday. Soc.* **57**, 1191 (1961).
11.* A Gangulee, P. S. Ho, and K. N. Tu, eds., *Low Temperature Diffusion and Applications to Thin Films*, Elsevier, Lausanne (1975); also *Thin Solid Films* **25** (1975).
12.* J. M. Poate, K. N. Tu, and J. W. Mayer, eds., *Thin Films—Interdiffusion and Reactions*, Wiley, New York (1978).
13. D. Gupta, *Phys. Rev.* **7**, 586 (1973).
14. D. Gupta and K. W. Asai, *Thin Solid Films* **22**, 121 (1974).
15. P. M. Hall, J. M. Morabito, and J. M. Poate, *Thin Solid Films* **33**, 107 (1976).
16. K. N. Tu, W. K. Chu, and J. W. Mayer, *Thin Solids Films* **25**, 403 (1975).
17.* K. N. Tu, *Ann. Rev. Mater. Sci.* **15**, 147 (1985).
18.* D. Gupta and P. S. Ho, *Thin Solid Films* **72**, 399 (1985).
19. J. C. M. Hwang, J. D. Pan, and R. W. Balluffi, *J. Appl. Phys.* **50**, 1349 (1979).
20. S. U. Campisano, G. Foti, R. Rimini, and J. W. Mayer, *Phil. Mag.* **31**, 903 (1975).
21. M. Ohring and R. Rosenberg, *J. Appl. Phys.* **42**, 5671 (1971).
22. S. Vaidya, T. T. Sheng, and A. K. Sinha, *Appl. Phys. Lett.* **36**, 464 (1980).
23. K. Nakamura, M.-A. Nicolet, J. W. Mayer, R. J. Blattner, and C. A. Evans, *J. Appl. Phys.* **46**, 4678 (1975).
24. G. Ottavio, *J. Vac. Sci. Tech.* **16**, 1112 (1979).
25. M.-A. Nicolet, *Thin Solid Films* **52**, 415 (1978).
26. M. Wittmer, *J. Vac. Sci. Tech.* **A2**, 273 (1984).
27. A. S. Grove, *Physics and Technology of Semiconductor Devices*, Wiley, New York (1967).
28. L. E. Katz, in *VLSI Technology*, 2nd ed., ed. S. M. Sze, McGraw-Hill, New York (1988).

*Recommended texts or reviews.